PAPER • OPEN ACCESS

Doping and alloying of kesterites

To cite this article: Yaroslav E Romanyuk *et al* 2019 *J. Phys. Energy* **1** 044004

View the article online for updates and enhancements.

You may also like

JPhys Energy

PAPER

Doping and alloying of kesterites

Yaroslav E Romanyuk[1] , **Stefan G Haass**[1], **Sergio Giraldo**[2], **Marcel Placidi**[2], **Devendra Tiwari**[3], **David J Fermin**[3] , **Xiaojing Hao**[4], **Hao Xin**[5], **Thomas Schnabel**[6], **Marit Kauk-Kuusik**[7], **Paul Pistor**[8], **Stener Lie**[9] and **Lydia H Wong**[9]

[1] Laboratory for Thin Films and Photovoltaics, Empa-Swiss Federal Laboratories for Materials Science and Technology, Ueberlandstr. 129, 8600 Dübendorf, Switzerland
[2] Catalonia Institute for Energy Research (IREC), Jardins de les Dones de Negre 1, 08930 Sant Adrià de Besòs, Barcelona, Spain
[3] School of Chemistry, University of Bristol, Bristol BS8 1TS, United Kingdom
[4] School of Photovoltaic and Renewable Energy Engineering, University of New South Wales, Sydney, Australia
[5] Key Laboratory for Organic Electronics and Information Displays & Jiangsu Key Laboratory for Biosensors, Nanjing University of Posts & Telecommunications, 9 Wenyuan Road, Nanjing 210023, People's Republic of China
[6] Zentrum für Sonnenenergie- und Wasserstoff- Forschung Baden-Württemberg, Meitnerstraße 1, 70565 Stuttgart, Germany
[7] Department of Materials and Environmental Technology, Tallinn University of Technology, Ehitajate tee 5, 19086 Tallinn, Estonia
[8] Martin Luther University Halle-Wittenberg, Institute of Physics, Von-Danckelmann-Platz 3, 06120 Halle (Saale), Germany
[9] School of Materials Science & Engineering, Nanyang Technological University, 639798 Singapore, Singapore

E-mail: yaroslav.romanyuk@empa.ch

Abstract

Attempts to improve the efficiency of kesterite solar cells by changing the intrinsic stoichiometry have not helped to boost the device efficiency beyond the current record of 12.6%. In this light, the addition of extrinsic elements to the $Cu_2ZnSn(S,Se)_4$ matrix in various quantities has emerged as a popular topic aiming to ameliorate electronic properties of the solar cell absorbers. This article reviews extrinsic doping and alloying concepts for kesterite absorbers with the focus on those that do not alter the parent zinc-blende derived kesterite structure. The latest state-of-the-art of possible extrinsic elements is presented in the order of groups of the periodic table. The highest reported solar cell efficiencies for each extrinsic dopant are tabulated at the end. Several dopants like alkali elements and substitutional alloying with Ag, Cd or Ge have been shown to improve the device performance of kesterite solar cells as compared to the nominally undoped references, although it is often difficult to differentiate between pure electronic effects and other possible influences such as changes in the crystallization path, deviations in matrix composition and presence of alkali dopants coming from the substrates. The review is concluded with a suggestion to intensify efforts for identifying intrinsic defects that negatively affect electronic properties of the kesterite absorbers, and, if identified, to test extrinsic strategies that may compensate these defects. Characterization techniques must be developed and widely used to reliably access semiconductor absorber metrics such as the quasi-Fermi level splitting, defect concentration and their energetic position, and carrier lifetime in order to assist in search for effective doping/alloying strategies.

1. Introduction

Kesterite materials—Cu_2ZnSnS_4 (CZTS), $Cu_2ZnSnSe_4$ (CZTSe), $Cu_2ZnSn(S,Se)_4$ (CZTSSe) are multinary compounds that can be synthesized in different off-stoichiometric compositions and therefore offer rich possibilities for defect engineering. According to the compositional classification of Lafond *et al* [1] that was further extended by Gurieva *et al* [2], up to 12 compositional-type materials can be distinguished, each of them corresponding to different cationic distribution giving rise to most probable secondary phases and intrinsic point defects. The highest efficiency solar cells are obtained, regardless of the kesterite absorber synthesis method, for Cu-poor, Sn-stoichiometric and Zn-rich compositions located around the so-called 'A' compositional line. The record 12.6%-efficient [3] (or 12.7% by improving emitter [4]) CZTSSe solar cell

demonstrated by the IBM group in 2014 had a targeted cation composition of $Cu/(Zn + Sn) = 0.8$ and $Zn/Sn = 1.1$ and did not include any intentional doping, although the presence of small quantities of alkali elements stemming from the soda-lime glass (SLG) substrate could not be excluded.

From the numerous combinatorial studies performed since the pioneering report of Katagiri in 2005 [5], it became clear that just by changing the absorber stoichiometry it was not possible to further advance the device performance. Thus, addition of *extrinsic* elements to the kesterite matrix in various quantities has emerged as a popular topic aiming to ameliorate electronic properties of the kesterite absorbers. This trend has also been inspired by the related CIGS and CdTe technologies, where the use of extrinsic species to passivate intrinsic defects and provide shallow dopants was combined with the bandgap engineering through substitutional doping (alloying) to boost the solar cell efficiencies beyond 22%.

This article aims to review *extrinsic* doping and alloying concepts for the kesterite absorbers, although in most (all) cases, a *combination* of the intrinsic and extrinsic defects will determine the final absorber properties. The review is limited to the extrinsic elements that *do not alter* the parent zinc-blende derived crystal structure of kesterites where all atoms have tetrahedral coordination.

1.1. Intrinsic doping

Before reviewing extrinsic elements, it is necessary to recall electronic properties of the non-intentionally doped kesterites, which have been summarized in several reviews [6, 7]. For the samples without secondary phases, numerous native lattice defects exist including Cu, Zn, Sn or S(Se) vacancies, (V_{Cu}, V_{Zn}, V_{Sn} and V_S or V_{Se}), interstitials (Cu_i, Zn_i, Sn_i and $S(Se)_i$), as well as antisites (Cu_{Zn}, Zn_{Cu}, Zn_{Sn}, Sn_{Zn}, etc). Besides these, the donor and acceptor defects may also compensate and attract each other, forming defect clusters ($V_{Cu} + Zn_{Cu}$, $2Cu_{Zn} + Sn_{Zn}$, $Zn_{Sn} + 2Zn_{Cu}$).

CZTS, CZTSe and CZTSSe samples have been widely found to show the p-type (hole mediated) conductivity intrinsically, while n-type samples have not been reported. The p-type conductivity is attributed to a high population of shallow acceptor-like defects such as Cu vacancies (V_{Cu}) and Cu_{Zn} antisites, whose density depends on the $Cu/(Zn + Sn)$ and Zn/Sn ratio. Despite the certainty of the p-type character, the reported hole concentrations from different experiments vary significantly, spanning a range from 1.2×10^{15} to 3.1×10^{20} cm^{-3} [6]. Three factors may contribute to the significant variation in the carrier concentration numbers including the presence of secondary phases (e.g. $Cu_2(S,Se)$ or $Zn(S,Se)$), deviations in the cationic ratios of $Cu/(Zn + Sn)$ and Zn/Sn, uncertainties of different measurement techniques and often unintended doping by elements such as Na from the glass substrate.

The doping concentration is typically deduced from capacitance–voltage (C–V) measurements of complete solar cell devices, where the acceptor concentration N_A can be calculated from the Mott–Schottky plots assuming an n$^+$p-type heterojunction. The obtained N_A values, however, can be affected by several non-idealities such as an inhomogeneous doping profile and contributions from deep defects [8, 9]. The C–V sweep of the 12.6% device resulted in the concentration $N_A \sim 2 \times 10^{16}$ cm^{-3} at zero bias [3]. The drive level capacitance profiling (DLCP) of the same sample, which should be sensitive only to bulk defects, yielded somewhat lower drive level densities of $< 7 \times 10^{15}$ cm^{-3}. Similar values have been frequently reported and can be used as reference points when reviewing the doping densities induced by extrinsic dopants in the following sections.

Another important semiconductor metric is the minority carrier lifetime that influences the carrier diffusion length and eventually limits the solar cell efficiency. Time-resolved photoluminescence (TRPL) is frequently employed to compare different kesterite absorbers whereby the measured PL decay time on the order of 1…10 ns is often associated with the minority carrier lifetime of the material. However, the reported lifetime values should be treated with precautions. It has been analyzed by Hages *et al* [10] that the PL decay times in kesterite materials are strongly influenced by minority carrier trapping, surface effects and energetic relaxation, and therefore *do not correspond* to the effective minority carrier lifetimes. With this in mind, the present article does not contain detailed discussions on reported PL time decays but suggests a need to develop more precise techniques for accessing minority carrier lifetime.

1.2. Extrinsic elements in this review

Figure 1 illustrates the extrinsic elements covered in this review. Depending on the concentration of the impurity element in the kesterite matrix, two cases can be distinguished: *doping* and *alloying*. These namings are not strict scientific terms (e.g. 'alloying' is often reserved for metallic alloys only whereas doping usually refers to a change in charge carrier density or type by introducing acceptor or donor states) but both terms have been widely adopted by the kesterite community. The doping elements are marked in blue, and the elements that can form substitutional alloying are shown in orange. For some elements, e.g. Li or Ge, both doping and alloying are considered.

Figure 1. Doping and alloying elements covered in this article.
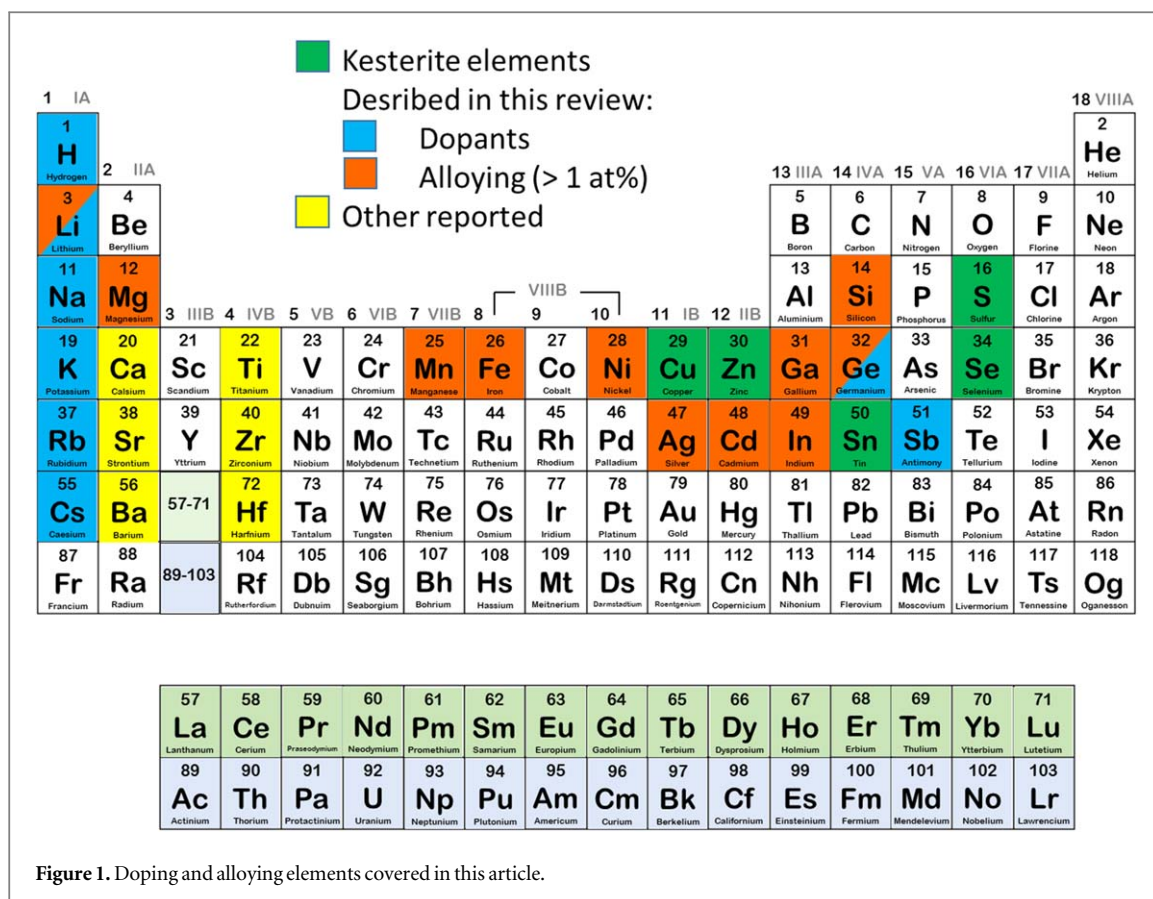
The purpose of doping is to change electronic, electrical, charge transport and interface properties without changing the crystal structure and altering the optical properties of the host material. In contrary, alloying is referred to an isoelectronic cation substitution to introduce ionic size mismatch, which can be particularly interesting for band engineering of the absorber. In this article, the term alloying is used if the concentration of extrinsic element can exceed 1 mol. % without changing the parent kesterite structure. Both doping and alloying effect can also be combined. For instance, both doping and alloying strategies have been crucial to reach very high efficiencies in CIGS cells, with the use of alkali elements for doping and alloying with Ga for band grading [11].

Extrinsic dopants can be divided into isoelectronic (i.e. with oxidation states matching to the replaced matrix element) and non-isoelectronic ones (e.g. Group III elements). There have been also other elements reported to replace Zn for Be, Ca [12, 13], Sr [14] or Ba [15, 16] and Sn for Ti, Zr, or Hf [17], but these will not be covered in this review as some of them, e.g. Ba, lead to the change of the kesterite crystal structure. When comparing ionic radii of the matrix and doping elements, crystal (ionic) radii for the tetrahedral coordination are taken from Shannon's tables [18], also other radii scales can also be used.

2. Group I elements

2.1. Hydrogen (H)

Hydrogen has been widely accepted as an effective passivation element for Si. In recent advanced hydrogenation technology, the photon-modulated charge state of hydrogen leads together with the heat treatment to an effective passivation of defects [19]. Similar to Si, in most semiconductors (e.g. GaAs, GAP, InP, and ZnSe) hydrogen impurities, being an amphoteric center, do not produce free carriers, yet hydrogen does dope chalcopyrite [20]. Hydrogen has been experimentally demonstrated to cause p-to-n conductivity-type conversion in $CuInSe_2$ through ion implantation [21]. This was further confirmed by first principle calculations [20] shown in figure 2. The calculations show that the effect of hydrogen in nonstoichiometric chalcopyrite (containing V_{Cu} and/or $III_{Cu} + 2V_{Cu}$) depends on the interplay between passivation of acceptor-like defects (i.e. $(V_{Cu} + H)^0$, hydrogen resides next to copper vacancy) and n-type doping (i.e. pairing of H^+ with $(III_{Cu} + 2V_{Cu})^0$).

Recently, Hao *et al* reported the potential passivation role of hydrogen in pure sulfide kesterite [22]. Hydrogen was introduced into the surface region of kesterite through the atomic layer deposition (ALD) of
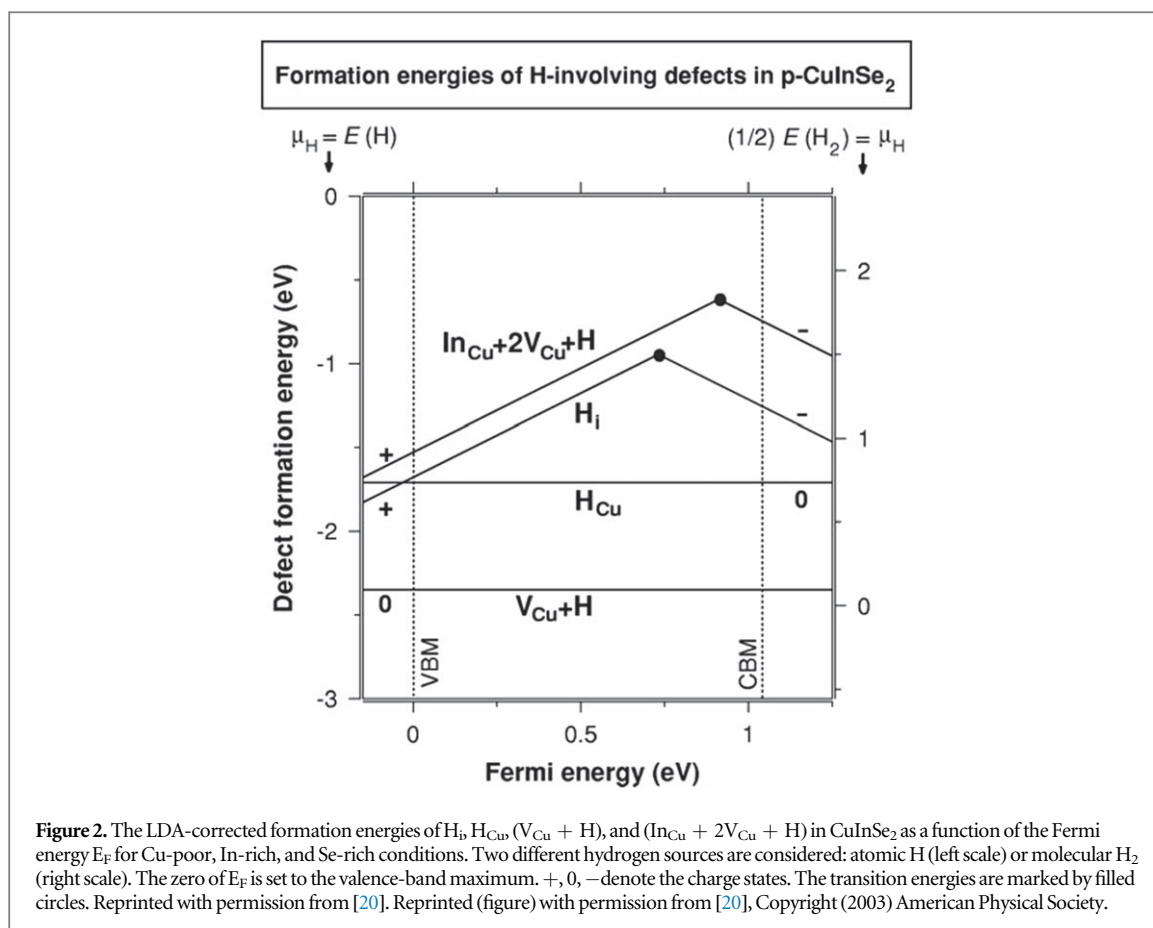
Figure 2. The LDA-corrected formation energies of H_i, H_{Cu}, $(V_{Cu} + H)$, and $(In_{Cu} + 2V_{Cu} + H)$ in CuInSe$_2$ as a function of the Fermi energy E_F for Cu-poor, In-rich, and Se-rich conditions. Two different hydrogen sources are considered: atomic H (left scale) or molecular H$_2$ (right scale). The zero of E_F is set to the valence-band maximum. $+$, 0, $-$ denote the charge states. The transition energies are marked by filled circles. Reprinted with permission from [20]. Reprinted (figure) with permission from [20], Copyright (2003) American Physical Society.
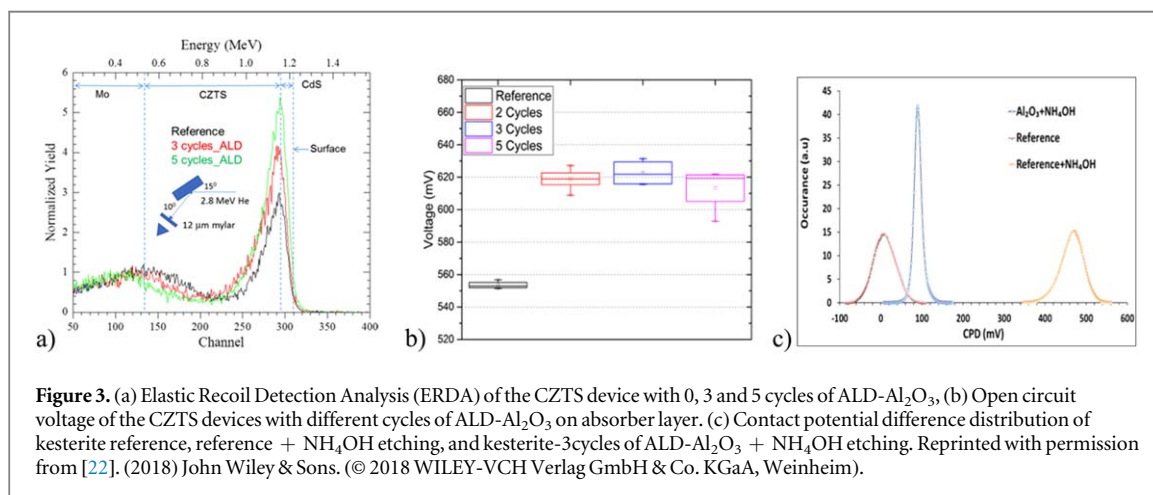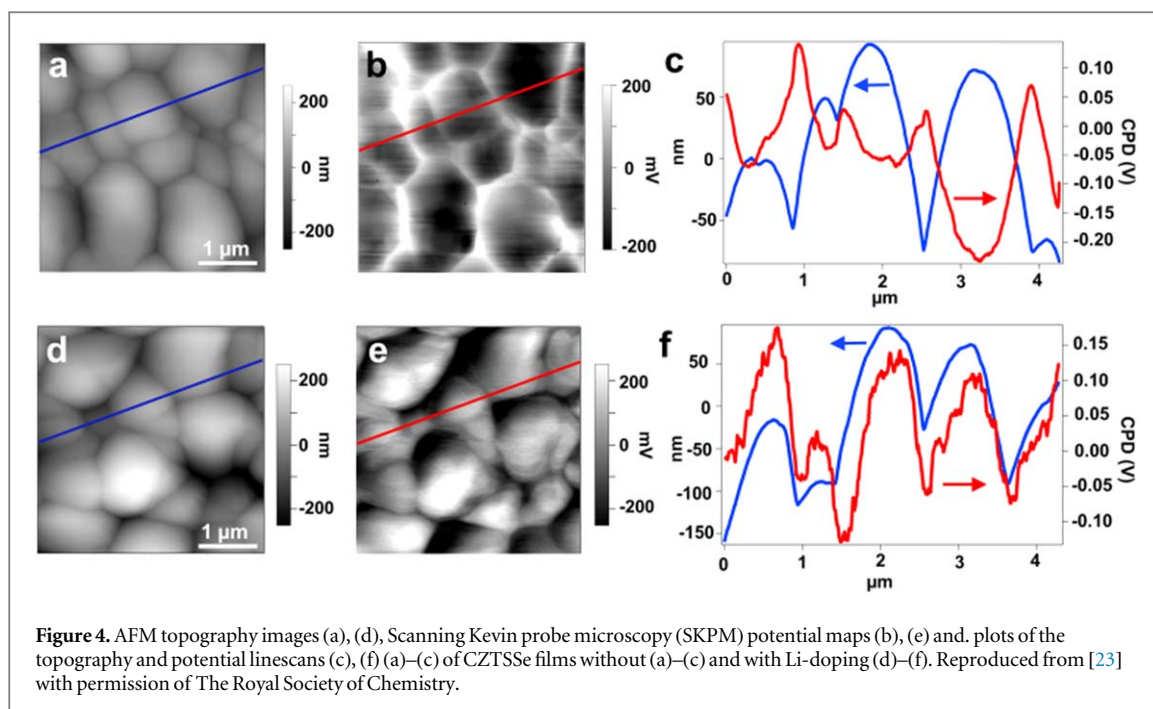

Figure 3. (a) Elastic Recoil Detection Analysis (ERDA) of the CZTS device with 0, 3 and 5 cycles of ALD-Al$_2$O$_3$, (b) Open circuit voltage of the CZTS devices with different cycles of ALD-Al$_2$O$_3$ on absorber layer. (c) Contact potential difference distribution of kesterite reference, reference $+$ NH$_4$OH etching, and kesterite-3cycles of ALD-Al$_2$O$_3$ $+$ NH$_4$OH etching. Reprinted with permission from [22]. (2018) John Wiley & Sons. (© 2018 WILEY-VCH Verlag GmbH & Co. KGaA, Weinheim).

Al$_2$O$_3$ on kesterite (see figure 3). Though no Al was detected by XPS, the open circuit voltage (V$_{OC}$) of completed kesterite devices was improved by about 70 mV. Additionally, their Kelvin probe force microscopy (KPFM) measurements revealed the passivation effect from hydrogen, where the contact potential difference of kesterite with incorporated hydrogen from ALD had a significantly different profile from that of the reference. The ALD Al$_2$O$_3$-treated samples exhibited a much smoother contact potential difference (CPD) profile (less CPD variation between grain boundary and grain interior) and much narrower CPD distribution than the kesterite reference. It was speculated that the hydrogen atom could bond with sulfur anions having dangling bonds at the grain boundaries. To clarify the effect of hydrogen in terms of its location in the kesterite lattice, detailed first principle calculations are required.

2.2. Lithium (Li)

The ionic radius of Li$^+$ (0.73 Å) is very close to that of Cu$^+$ (0.74 Å), and thus has the highest probability to be incorporated into the lattice of kesterite phase and affect the photovoltaic properties compared to heavier alkali

Figure 4. AFM topography images (a), (d), Scanning Kevin probe microscopy (SKPM) potential maps (b), (e) and. plots of the topography and potential linescans (c), (f) (a)–(c) of CZTSSe films without (a)–(c) and with Li-doping (d)–(f). Reproduced from [23] with permission of The Royal Society of Chemistry.

elements. Surprisingly, the studies on Li doping/alloying on CZTS are quite recent. In 2015, Xin *et al* [23] first reported Li doping in dimethyl sulfoxide (DMSO) precursor solution processed CZTSSe absorber by adding the Li salts directly into the solution. A dramatic change in the electronic property of the CZTSSe upon Li doping was found although the Li concentration in the final film was very low (Li/Cu $= 3.9 \times 10^{-5}$). The conductivity of the doped film was improved by one order of magnitude and the electrical potential at grain boundaries was reversal to the non-doped one (figure 4) which results in an upward band bending and reduces recombination by repelling minority carriers from the detrimental defect rich grain boundaries. The performance of CZTSSe solar cells was improved by more than 30% to an active-area efficiency of 11.8%.

Yang *et al* [24] demonstrated that Li incorporates into the lattice of CZTSSe and tunes the band gap of $Li_xCu_{2-x}ZnSn(S,Se)_4$ without significant effect on carrier concentration and crystal growth [25] when films were selenized on quartz substrates. Later, they reported [26] that only traces of Li (Li/Cu $= 3.4 \times 10^{-4}$) were left in the final CZTSSe film when the films were fabricated on SLG substrates. A Li/Na exchange mechanism was proposed for the observed phenomenon. The Li alloying and band gap tuning are also achieved by Lafond *et al* [25] from a ceramic synthesis route. Cabas-Vidani *et al* [27] confirmed the lithium alloying in the kesterite thin films $(Li_xCu_{1-x})_2ZnSn(S,Se)_4$ in the range x $= 0$ to 0.12 as measured by inductively coupled plasma mass spectrometry (ICP-MS), and a widening of the bandgap from 1.05 to 1.18 eV was observed. Morphology improvement and apparent carrier concentration increase from 3×10^{15} cm^{-3} to 5×10^{16} cm^{-3} was observed when increasing x from 0 up to 0.07, and a corresponding device had an active area efficiency of 12.2%. In a comprehensive study on the effects of all alkali elements in CZTSSe, Haass *et al* [28] found that Li is the most favorable among all alkalis, it improves the crystallization and it requires a comparatively high Sn/ (Cu $+$ Zn $+$ Sn) content for the maximum device efficiency. The apparent carrier concentration estimated from C-V measurements varied in a broad range $10^{15}\ldots10^{18}$ cm^{-3} when changing (decreasing) the Sn content yet keeping the same Li content, indicating that the *intrinsic* doping rather prevails. A champion device with 11.5% efficiency (12.3% active area) was achieved using a 'high' Li concentration of 0.75 at% at an optimized Sn content.

Although the results and the explanation on the effect of Li doping/alloying differ and even contrast to each other, partially due to variation in material preparation conditions and matrix composition, some conclusions can be drawn based on the available reports [23–32]: (1) Li alloys with CZTS and widens the band gap of $(Li_xCu_{1-x})_2ZnSn(S,Se)_4$ [24, 25, 27]; (2) incorporation of Li to kesterite is sensitive to Na so that Li alloying is more easily achieved without Na, in the ceramic route [25] or on quartz substrate, or using a blocking layer to prevent Na diffusion from SLG [24, 27]. The presence of Na diffused from SLG greatly reduces the Li doping concentration [23, 26]; (3) Li doping/alloying improves photovoltaic performance regardless the doping concentration, however, the mechanism on how Li doping/alloying improves device performance remains unclear.
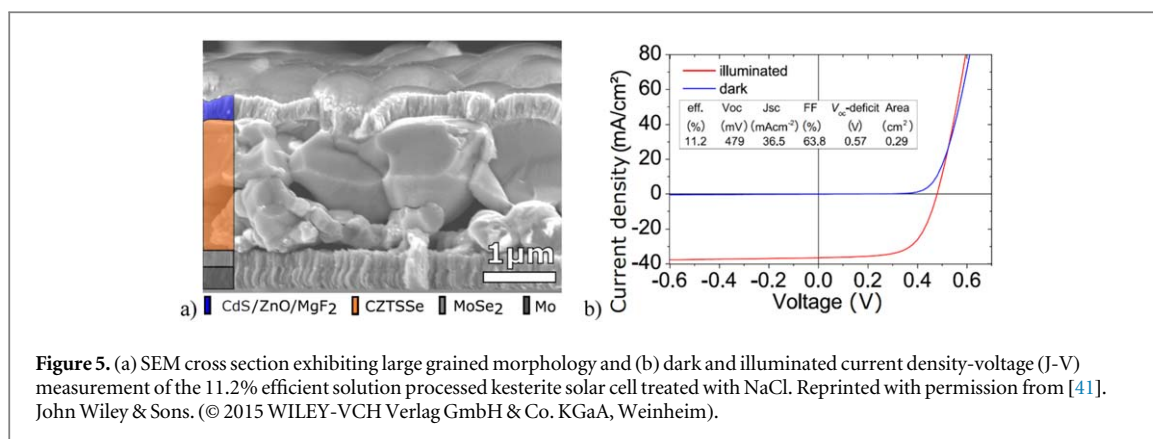
Figure 5. (a) SEM cross section exhibiting large grained morphology and (b) dark and illuminated current density-voltage (J-V) measurement of the 11.2% efficient solution processed kesterite solar cell treated with NaCl. Reprinted with permission from [41]. John Wiley & Sons. (© 2015 WILEY-VCH Verlag GmbH & Co. KGaA, Weinheim).

2.3. Sodium (Na)

Since the early 1990's, it is known that Na leads to significant improvements on CIGS solar cells [33]. For kesterite solar cells, the effects of Na were thoroughly investigated [34–37] and it has been shown that Na diffusion from SLG has similar positive effects on absorber morphology and device properties in kesterite devices [37, 38]. Na treatment increases grain size and improves the overall absorber layer morphology, increases doping concentration and was shown to yield improved opto-electronic properties of the absorber layer. The increased grain size is attributed to the capability of Na to form low-temperature Na_2Se_x liquid phases [37] that act as a fluxing agent and facilitate grain growth. The improvements of opto-electronic properties are associated with the passivation of defects at grain boundaries and interfaces, which are the predominant locations for Na inside the absorber layer [30]. Atom probe tomography (APT) measurements revealed that the sodium concentration in the grain interior is only about 20% of what is measured by ICP-MS in the absorber layer, which supports the assumption that sodium is primarily segregated at the grain boundaries and absorber surface [39].
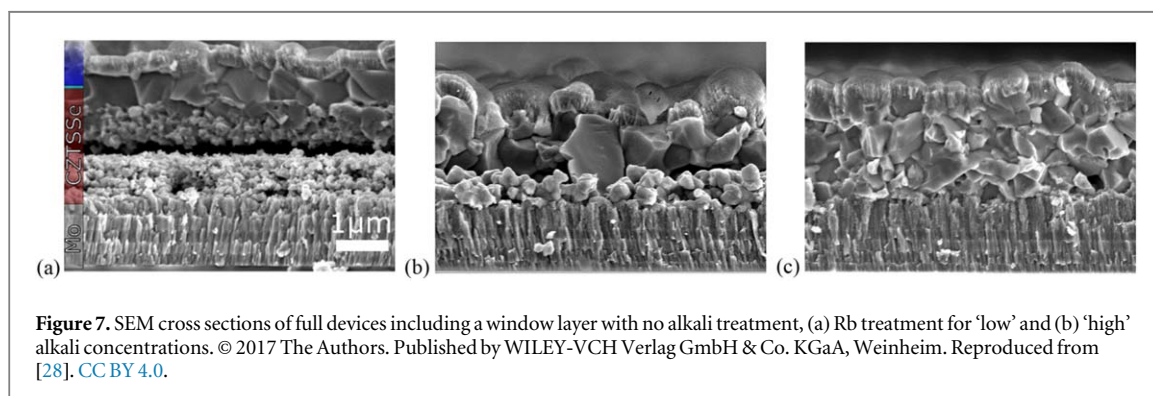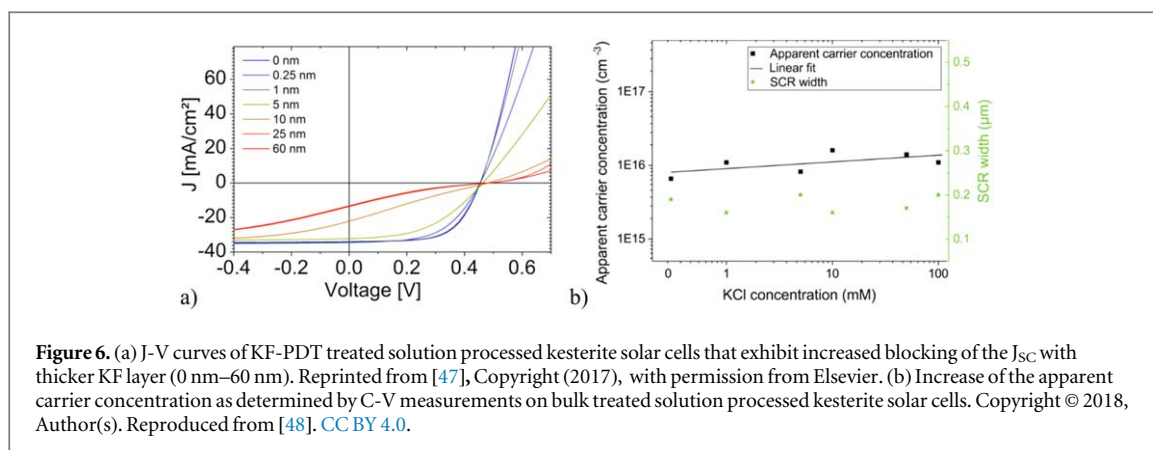
NaCl treatment of solution-processed kesterite solar cells was investigated by Sutter-Fella and Werner [37, 40], who showed that a tailored addition of Na improves grain growth and optoelectronic properties, especially open-circuit voltage V_{OC} and fill-factor *FF*. However, only a fraction of the added sodium is eventually incorporated into the processed absorber layer, e.g. adding nominally 3.33 at% NaCl resulted in only 0.18 at% in the processed absorber layer as determined by ICP-MS measurements [28]. An 11.2%-efficient CZTSSe solar cell is fabricated using NaCl treatment (figure 5) and the device features a V_{OC} - deficit (defined as $Eg/e − V_{OC}$) of only 0.57 V, which is amongst the lowest for kesterite solar cells [41]. The reduced V_{OC} - deficit is attributed to a low diode saturation current and ideality factor, which are signatures of the semiconductor material with a low concentration of recombination centers. Even a higher efficiency of 11.6% was obtained for a Na-doped CZTSe absorber grown by thermal co-evaporation [42], proving the effectiveness of the Na doping.

2.4. Potassium (K)

Based on its chemistry, K could be located on the Cu positions within the kesterite lattice, however, previous studies about the localization of potassium in chalcogenide absorber layers by APT revealed that potassium is segregating at the grain boundaries [43, 44]. Due to the large size of 1.51 Å of the K + ion and thus a high substitution energy of 1.53 eV, alloying of potassium within the kesterite lattice is unlikely [30]. Potassium addition can enhance the (112) preferred orientation and reduce ZnS secondary phases in solution-processed CZTS absorber layers [45]. For solar cell devices, a reduction in the series resistance was observed upon potassium addition [45] whereas the carrier concentration could be increased for potassium as compared to untreated samples [32, 46]. Potassium is a potent agent to promote grain growth during the absorber layer synthesis.

Potassium treatment of kesterite solar cells can be conducted using two main approaches: the potassium-fluoride post deposition treatment (KF-PDT) [47] and the bulk treatment [48]. KF-PDT of solution-processed kesterite solar cells with various KF thicknesses exhibits a decrease in short-circuit current density J_{SC}, *FF* and efficiency with increasing KF thickness, which originates from a severe blocking of the photocurrent (figure 6(a)). The CdS buffer layer growth is not affected by KF-PDT, but the buffer layer exhibits a photoconductivity effect in external quantum efficiency (EQE) measurements. Although KF-PDT improves the V_{OC}, it is evident that the surface chemistry does not yield a beneficial interface layer and thus, no performance improvements can be observed [47].

The K bulk treatment of kesterite solar cells leads to an enhanced grain growth and improved photovoltaic (PV) properties resulting in devices close to 10% conversion efficiency. K is an effective fluxing agent and additionally suppresses incorporation of Na from the soda lime glass. Incorporation of high concentrations of K also reduces the loss of Sn, which results in a change of order/disorder of the Cu/Zn sub-lattice and thereby additionally widens the bandgap and increases the tetragonal distortion [48]. Potassium doping increases the

Figure 6. (a) J-V curves of KF-PDT treated solution processed kesterite solar cells that exhibit increased blocking of the J_{SC} with thicker KF layer (0 nm–60 nm). Reprinted from [47], Copyright (2017), with permission from Elsevier. (b) Increase of the apparent carrier concentration as determined by C-V measurements on bulk treated solution processed kesterite solar cells. Copyright © 2018, Author(s). Reproduced from [48]. CC BY 4.0.

Figure 7. SEM cross sections of full devices including a window layer with no alkali treatment, (a) Rb treatment for 'low' and (b) 'high' alkali concentrations. © 2017 The Authors. Published by WILEY-VCH Verlag GmbH & Co. KGaA, Weinheim. Reproduced from [28]. CC BY 4.0.

carrier concentration as derived from C-V measurements shown in figure 6(b). Higher nominal K concentrations require an adjustment of the Sn content in the absorber layer in order to avoid formation of $Sn(S,Se)_2$ secondary phase and thus deterioration of the device performance.
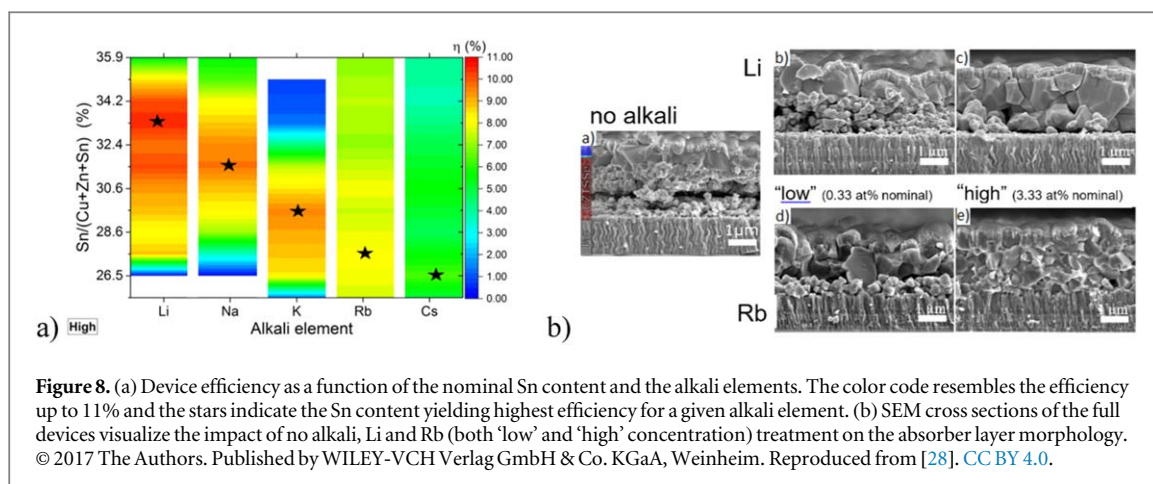
2.5. Rubidium (Rb) & caesium (Cs)

Rubidium and caesium are alkali elements with ionic radii of 1.66 Å and 1.81 Å, respectively, which is significantly larger than Cu with 0.74 Å. XRD measurements on Rb and Cs treated CZTSSe absorber layers indicated that Rb and even more so Cs are not replacing CZTSSe atoms in the kesterite lattice [32]. The impact of Rb and Cs on kesterite absorbers and respective device performance was studied several times [28, 29, 32]. Equivalent to the lighter alkali metals, Rb and Cs can form alkali poly-selenide liquid phases at comparably low temperatures. These liquid phases act as a fluxing agent during the selenization process and improve grain size and the overall absorber layer morphology. However, a too high concentration leads to the fragmentation of the absorber layer and a dense but small-grained morphology with a high density of grain boundaries (figure 7). Rb and Cs treated samples exhibit a large-grain morphology for 'low' nominal alkali concentration, whereas a 'high' alkali content results in a small-grain morphology. The final device efficiencies are correlated with the absorber layer morphology, and the highest efficiency of 8.8 and 9.1% were obtained for Rb and Cs, respectively, for 'low' concentration of ca. 0.15 at% (relative to all elements, as measured by ICP-MS) [28]. It is not clear how much of Rb and Cs are located inside the kesterite grains so it is assumed that most of them reside at grain boundaries.

2.6. Comparison of alkali elements

Several studies comparing different alkali elements and their effects on kesterite properties and device performance have been published [29, 31, 32, 49]. However, no consistent experimental results have been obtained concerning the impact of alkali treatments on the device properties and performance. A study by Haass *et al* [28] revealed that each alkali element requires a different absorber composition to achieve the highest PV performance (figure 8(a)). From Li to Cs the nominal Sn concentration (Sn/Cu + Zn + Sn) required for best device performance should be reduced by more than 20% (relative).

The alkali concentration yielding the best devices for Li (11.1% efficiency), Na (10.0%) and K (10.0%) is 10 times higher compared to optimum alkali concentration for Rb (8.8%) and Cs (9.1%). ICP-MS measurements show that the alkali content in the kesterite layer is proportional to the nominal input, however, light dopants like Li tend to be lost during the processing steps (in the case of spin-coated precursor solutions). As the alkali elements

Figure 8. (a) Device efficiency as a function of the nominal Sn content and the alkali elements. The color code resembles the efficiency up to 11% and the stars indicate the Sn content yielding highest efficiency for a given alkali element. (b) SEM cross sections of the full devices visualize the impact of no alkali, Li and Rb (both 'low' and 'high' concentration) treatment on the absorber layer morphology. © 2017 The Authors. Published by WILEY-VCH Verlag GmbH & Co. KGaA, Weinheim. Reproduced from [28]. CC BY 4.0.

are preferably located along the grain boundaries [50, 51], the overall amount measured by ICP-MS, which does not discriminate between alkali elements inside grains or at the grain boundaries, is expected to be higher for samples with a higher density of grain boundaries.

The morphology for each alkali element and concentration indicates that the lighter alkali elements require a higher concentration to reach a similar improvement in morphology as compared to the heavier alkali elements. This could be due to lower melting points for alkali-poly-selenide phases of heavier alkali species as compared to lighter ones [52–56]. Because of the lower melting points the heavier alkali elements act more efficiently as a fluxing agent and, hence, lower concentrations are required to achieve similar grain size improvements.
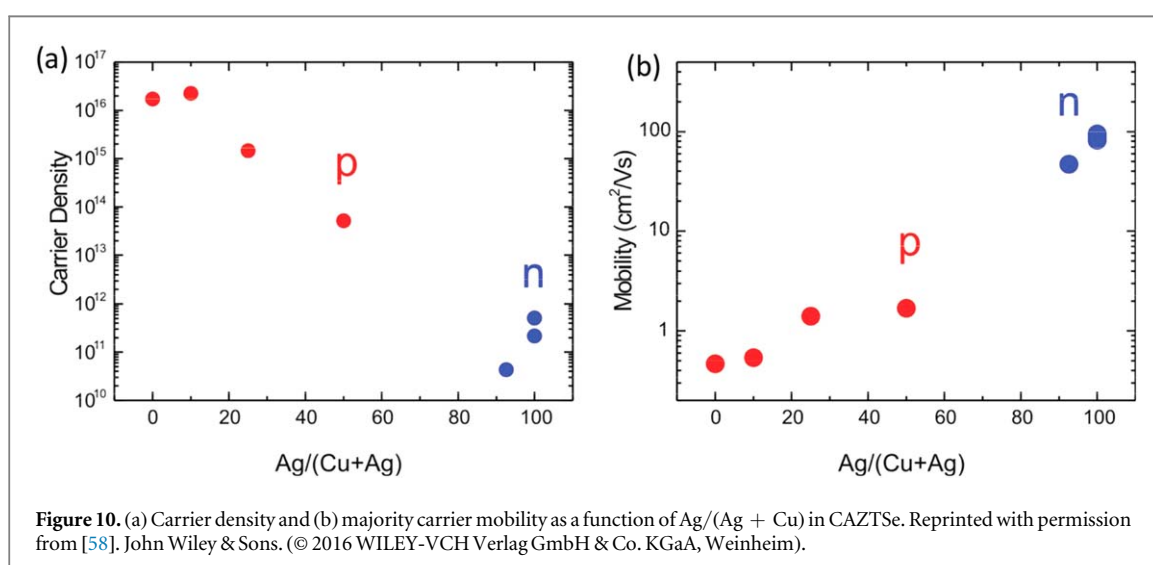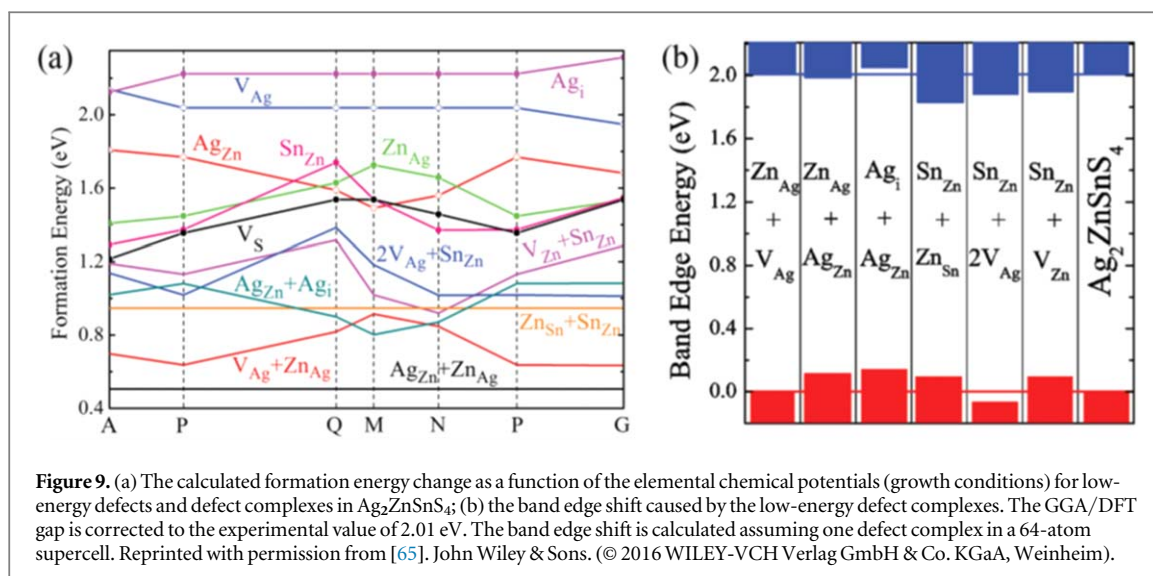
The PV parameters correlate with the changes in morphology with best devices exhibiting large grains throughout the whole absorber layer with a low density of grain boundaries (figure 8(b)). The formation of $Sn(S,Se)_2$ secondary phase is increased for the heavier alkali elements and for 'high' concentrations. As revealed by EQE and C-V measurements the apparent carrier concentration varies by three orders of magnitude depending on the Sn content, except for high Rb and Cs content where a constant kesterite composition and therefore constant apparent carrier concentration is observed. A ranking of best device performances employing alkali treatment resulted in the order of Li > Na > K > Rb > Cs based on the statistics of more than 700 individual cells.

TRPL measurements of numerous alkali-containing devices yielded PL decay times in the range 1…8 ns but no correlation between PL decay time and efficiency, or decay time and alkali ionic radii could be detected [57]. That is in line with the observations of Hages *et al* [10], who conclude that the minority carrier trapping can severely alter (extend) measured PL transient times.

2.7. Silver (Ag)

One of the most explored methods to improve the efficiency of CZTS solar cell is partial substitution of Cu by Ag. The increase in V_{OC} on both CZTS or CZTSe is evident in most of the reported studies [58–62]. This strategy was theoretically proposed as an effective method to reduce the concentration of Cu_{Zn} antisite pairs [63, 64]. The substantially higher crystal radius of Ag^+ (1.14 Å) compared to Cu^+ (0.74 Å) contributes to the higher formation energy of antisite defects and Ag-related defect complexes such as $Ag_{Zn} + Zn_{Ag}$ and $2Ag_{Sn} + Sn_{Zn}$ in Ag_2ZnSnS_4 (AZTS) based on theoretical calculations [18, 65–67] (figure 9(a)). The lower valence band edge in AZTS (by 0.74 eV) also plays an important role in decreasing the amount of antisite defects [65]. However, it also increases the formation energy of the other acceptor defects which makes the intrinsically n-type AZTS difficult to be doped p-type. Besides the higher formation energy, the Ag- and Zn- related defects form shallow defects and consequently their defect cluster creates smaller band edge shifting compared to CZTS (see figure 9(b)). In the case of partial Ag substitution, low level (<6% Ag) Ag substitution is expected to suppress Cu-Zn disorder only under Cu-rich and constrained Cu-poor conditions (presence of ZnS, SnS, and Cu-deficient phases with Zn- and Sn-rich condition); meanwhile, at a high level (>6% Ag) Ag substitution, the disorder suppression is more effective because higher formation energy of antisite defects [68].

There are several experimental studies for $(Cu,Ag)_2ZnSn(S,Se)_4$ (CAZTSSe). $(Cu_{1-x}Ag_x)_2ZnSnS_4$ (CAZTS) and $(Cu_{1-x}Ag_x)_2ZnSnSe_4$ (CAZTSe) crystal powders with $0 \leqslant x \leqslant 1.0$ have been reported to have tetragonal kesterite structure based on Rietveld refinement analysis of XRD and bandgap from 1.5 to 2.01 eV for CAZTS and from 1.0 to 1.34 eV for CAZTSe [69]. Recently, another study using neutron and x-ray diffraction suggests that CAZTSe with $x = 0.17$ and 0.46 crystallize in the stannite type structure and thus suppress Cu/Zn disorder while the end members of the solid solution are reported to crystallize in the kesterite structure [70]. In terms of optoelectronic properties, Gershon *et al* reported reduction in band tailing from CZTSe to AZTSe based on the reduction of the band tailing parameter (γ) extracted from EQE with a value of ≈18 meV which is half of the one for CZTSe (≈33 meV) [71]. In

Figure 9. (a) The calculated formation energy change as a function of the elemental chemical potentials (growth conditions) for low-energy defects and defect complexes in Ag_2ZnSnS_4; (b) the band edge shift caused by the low-energy defect complexes. The GGA/DFT gap is corrected to the experimental value of 2.01 eV. The band edge shift is calculated assuming one defect complex in a 64-atom supercell. Reprinted with permission from [65]. John Wiley & Sons. (© 2016 WILEY-VCH Verlag GmbH & Co. KGaA, Weinheim).

Figure 10. (a) Carrier density and (b) majority carrier mobility as a function of Ag/(Ag + Cu) in CAZTSe. Reprinted with permission from [58]. John Wiley & Sons. (© 2016 WILEY-VCH Verlag GmbH & Co. KGaA, Weinheim).

addition, there is a change of majority carriers from p-type (for CZTSe) to n-type (for AZTSe) which is accompanied by a significant decrease in carrier concentration and increase in Hall mobility (see figure 10). They also first demonstrated a reduction in the V_{OC} deficit ($E_g/e - V_{OC}$) from about 660 to 580 mV and device performance improvement from 9% to 10.2% efficiency for the 10% Ag substituted CZTSe using a co-evaporation process [58]. Similar results for CAZTSe is also obtained through nanoparticle ink synthesis which achieved device improvement up to 7.2% for CAZTSe at 5% Ag substitution due to improved grain growth, improved minority carrier lifetime, reduced defect formation, and reduced potential fluctuations [60].

For sulfur-based CAZTS, Wong *et al* reported the first solar cell device improvement from 4.9% to 7.2% based on molecular method using metal salts precursor [59]. The power conversion efficiency for pure sulfide kesterite with Ag substitution was further improved to 8.3%, with the suppression of non-radiative defects as the main reason for this improvement [72]. The incorporation of Ag (<7 mol% of Ag/(Ag + Cu)) improved the grain size, increased the depletion width, decreased the charge carrier density, and improved the PL decay time from 1.9 ns for non-intentionally doped CZTS to 3.6 ns for 5 mol% Ag-doped [59, 72].

Similar results are also obtained for CAZTS (Ag/(Ag + Cu) of ca. 0.02) deposited by spray pyrolysis, where the use of an Ag-incorporated film improved the band alignment at the CdS–CZTS interface [73]. In that case the conduction band-offset at the absorber-buffer interface estimated from x-ray photoelectron spectroscopy and EQE measurements was reduced from −0.25 eV for the CdS-CZTS down to -0.17 eV for the CdS-CAZTS heterointerface [73].

Following these positive results, several synthesis strategies were explored to improve the Ag-substituted CZTSSe. Qi *et al* obtained the highest solar cell efficiency of 10.36% for CAZTSSe at 3% Ag substitution using a solution-based method [57]. They observed a reduction of the V_{OC} deficit from 727 mV (CZTSSe without Ag) to 601 mV (CAZTSe with 3 mol% Ag).

Another strategy of using Ag is by engineering the interface band bending and defect elimination, by placing a higher Ag content CAZTSSe at the back and front interface to create V-shape Ag-graded film [7, 62, 65]. The highest efficiency of 11.2% with a 110 mV V_{OC} enhancement was achieved due to the improvement of the distance between Fermi levels and conduction bands and decrease in Cu_{Zn} defects at the interface [61]. The energetic difference between the Fermi level and conduction band of the Ag-graded CdS/CAZTSSe heterojunction was estimated from ultraviolet photoelectron spectroscopy and PL measurements to be 100 mV smaller than that of the CdS/CZTSSe heterojunction [61]. To conclude, Ag substitution has shown encouraging results in tackling V_{OC} limitation in CZTS solar cell based on the experimental evidence of reduced band tailing parameter (γ), improved photoluminescence decay time, and better band level alignment at the interface.

3. Group II elements

3.1. Magnesium (Mg)
It was suggested that the substitution of Cu or Zn by other elements such as Mg could suppress the antisite defects Cu_{Zn} and/or Zn_{Cu} formation that limit kesterite solar cells performance [13]. Several studies about the Mg incorporation into kesterite have been published, but the observed effects of Mg are contradictory. For instance, Cu_2MgSnS_4 thin films grown by ultrasonic co-spray pyrolysis showed p-type conductivity and band-gap energy of 1.76 eV [74]. In contrary, n-type conductivity was estimated for $(Cu_{2-x}Mg_x)ZnSnSe_4$ bulk materials with x = 0.1–0.4, which was attributed to the formation of the donor-type Mg_{Cu} antisite defects [75]. The formation of stable $Cu_2MgSn(S,Se)_4$ was calculated based on the density functional theory [13], whereas a complete phase separation was predicted by [64].

Regarding solar cells with Mg incorporation, $Cu_2Zn_{1-x}Mg_xSn(S,Se)_4$ absorber layers with variable Mg concentration x = 0…1 were deposited using the solution approach [76]. For heavy Mg alloying with x = 0.55…1 the phase separation of Cu_2SnSe_3, $MgSe_2$, MgSe and $SnSe_2$ occurs in agreement with literature predictions [64], whereas a lower Mg concentration of x = 0.04 resulted in the kesterite phase. An apparent carrier concentration of $1 \times 10^{16}\,cm^{-3}$ was measured for Mg-doped kesterite solar cell device, confirming the *p*-type conductivity. Raman spectroscopy indicated that structural defects can be reduced in Mg-containing absorbers as compared to the dopant-free reference samples, resulting in the highest device efficiency of 7.2% for a Mg-doped cell measured in [76].

3.2. Cadmium (Cd)
Cd alloying of kesterite (CZCTS) was proposed to reduce the impact of Cu_{Zn} and Zn_{Cu} antisite defects. The formation of large population of Cu_{Zn} and Zn_{Cu} antisite defects is mainly due to the close cation sizes and chemical electronic properties of Cu^+ and Zn^{2+} in kesterite system [77]. Cd is in the same group with Zn and is expected to substitute Zn in the host lattice. As the ionic radius of Cd^{2+} (0.92 Å) is larger than that of Cu^+ and Zn^{2+} (both 0.74 Å), Cd is expected to increase the formation energy of Cu_{Cd} and Cd_{Cu} antisites defects, thereby suppressing the disorder and band tailing issues in kesterite system. In addition to the change in the defects system, replacing Zn by Cd can also facilitate the grain growth and suppress the secondary phase formation [78, 79]. Therefore, Cd alloying in kesterite has drawn considerable attention. According to the density functional theory (DFT) calculation, the role of Cd alloying depends on the Cd content in the system [68]. Low level of Cd substitution can alleviate the disorder in the Cu-Zn sublattice because of the increased formation energy of antisite defects, whilst high level of Cd substitution will be detrimental due to the transformation from the kesterite to stannite structure.

Wong *et al* reported significant device performance improvement by finely tuning the Zn/Cd ratio in CZTS using sol-gel method (figure 11(a)) [78]. The grain sizes of Cd alloyed CZTS increase substantially as the Cd/(Cd + Zn) ratio increases from 0 to 40%, but stop increasing from Cd concentration over 50%. Furthermore, phase transition from kesterite to stannite is revealed when Cd/(Cd + Zn) > 0.6, which agrees with the theoretical calculation results [68] and experimental study [80]. In addition, Wong *et al* also showed the suppression of ZnS secondary phases and the change of carrier density and related depletion region width due to the Cd alloying. With the optimized amount of Cd alloying, efficiency is significantly improved from 5.3% to 9.24% by controlling the Cd substitution at 40%.

Similar results were also observed by Hao *et al* [79], where the reported efficiency was further boosted to 11.5% by fixing the Cd substitution to 40% based on vacuum-based sputter method (figure 11(b)). Their work also showed the enlarged grain size and changed secondary phases with Cd-alloying. The band tailing problem in their work is studied by Urbach tail energy (E_{Urbach}) model which is characterized by photothermal deflection spectroscopy (PDS). The lower E_{Urbach} of CZCTS compared to CZTS indicates the reduced band tailing which is correlated to the decreased disorder resulting from Cu-Zn antisite defects. Additionally, the Cd alloying can also increase the minority carrier lifetime. As a result, the V_{OC}-deficit reduced by more than 100 mV after Cd substitution [79].
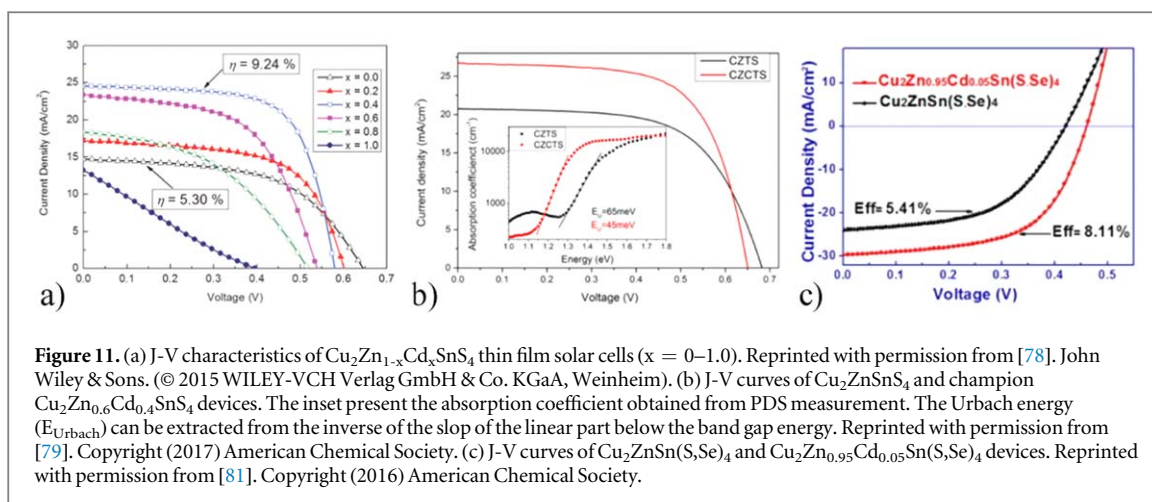
Figure 11. (a) J-V characteristics of $Cu_2Zn_{1-x}Cd_xSnS_4$ thin film solar cells (x = 0–1.0). Reprinted with permission from [78]. John Wiley & Sons. (© 2015 WILEY-VCH Verlag GmbH & Co. KGaA, Weinheim). (b) J-V curves of Cu_2ZnSnS_4 and champion $Cu_2Zn_{0.6}Cd_{0.4}SnS_4$ devices. The inset present the absorption coefficient obtained from PDS measurement. The Urbach energy (E_{Urbach}) can be extracted from the inverse of the slop of the linear part below the band gap energy. Reprinted with permission from [79]. Copyright (2017) American Chemical Society. (c) J-V curves of $Cu_2ZnSn(S,Se)_4$ and $Cu_2Zn_{0.95}Cd_{0.05}Sn(S,Se)_4$ devices. Reprinted with permission from [81]. Copyright (2016) American Chemical Society.

It is well known that the Se-containing kesterite solar cells present less V_{OC} deficit than that of pure sulfide [82, 83], which could possibly be attributed to the higher formation energy of Cu-Zn antisite defects in selenide kesterite [84]. In this case, the amount of Cd substitution can be controlled in a lower amount to obtain fewer antisite defects. Wu *et al* reported that the device performance of CZTSSe solar cell is improved from 5.41% to 8.11% by introducing only 5% Cd substitution in a solution method (figure 11(c)) [81]. The role of Cd alloying in promoting grain growth and changing charge density and depletion region width is also observed in this research. By controlling the Cd/(Cd + Zn) at 0.13, Sun *et al* achieved a CZTSSe solar cell with efficiency over 11% [85]. The Cd was incorporated by selenizing chemical bath deposited CdS on top of the sputtered quaternary CZTS precursors. Besides the grain size and carrier concentration change as reported previously, the trap energy level is estimated to be decreased after Cd alloying.

So far, CdS has been generally adopted as the buffer material for Cd-alloyed kesterite. For pure sulfide kesterite CZTS, $Zn_xCd_{1-x}S$ was showed as a potential buffer option [86]. Upon heat treatment of CZTS/CdS heterojunction, $Zn_xCd_{1-x}S/Cu_2Zn_xCd_{1-x}SnS_4$ heterointerface is formed as a result of elemental inter-diffusion, where slight Cd diffuses into the CZTS surface and Zn diffuses into CdS [86]. Hao *et al* reported that these elemental inter-diffusion at heterojunction facilitates the formation of a more favorable band alignment of $Zn_xCd_{1-x}S/Cu_2Zn_xCd_{1-x}SnS_4$, resulting in the suppression of the heterojunction interface recombination, which promotes the efficiency of pure sulfide CZTS to over 11% [86].
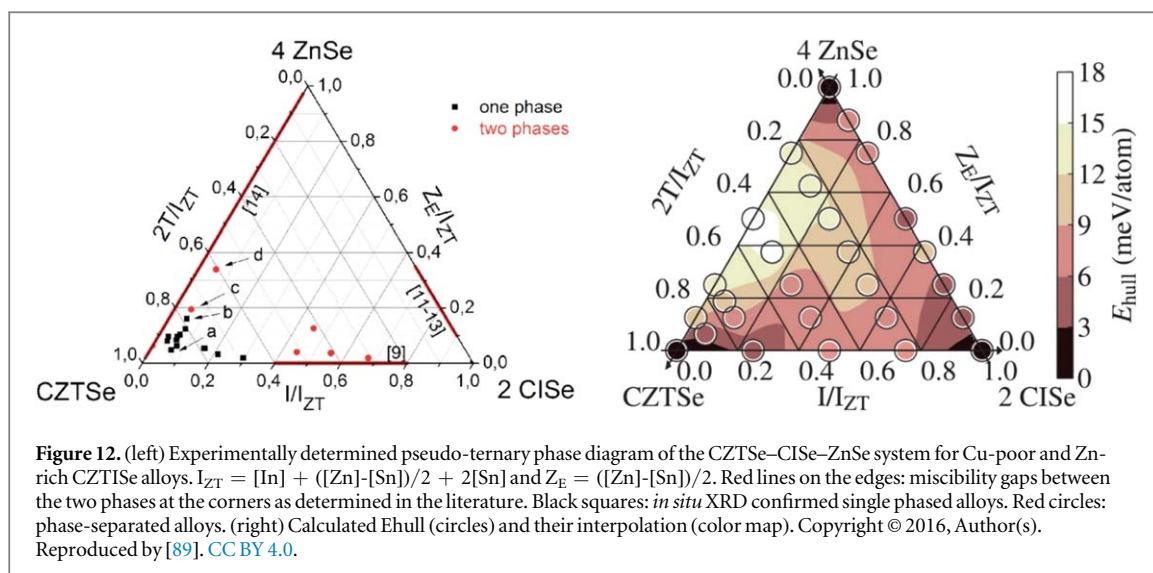
4. Group III

4.1. Indium (In) and gallium (Ga)

The crystal structure of kesterites is generally derived from the wurtzite crystal structure of ZnSe in the increasing series of complexity from $ZnSe–CuInSe_2–Cu_2ZnSnSe_4$ in the attempt to avoid the scarce materials In and Ga. However, the chalcopyrite ancestors of the kesterites based on $Cu(In,Ga)Se_2$ still outperform solar cells with kesterite absorbers by far. Despite the limitation in indium abundancy it is therefore interesting to evaluate mixtures in the $CuInSe_2$-$Cu_2ZnSnSe_4$ system and put their behavior in relation.

In recent experiments, Giraldo *et al* have processed CZTSe thin film absorbers by a sequential sputter and reactive annealing process [87] and studied the impact on performance of depositing small amounts of In (0–10 nm, corresponding to a maximum of up to nominal 2.6×10^{10} at cm^{-3}) onto the metallic precursor stacks prior to selenization. The efficiency of solar cell devices was slightly decreased, mainly by a small drop in *FF*, suggesting that CZTSe can tolerate incorporation of small amounts of In into the crystal structure, but devices did not particularly benefit from it.

Powders along the complete compositional range from $Cu_2ZnSnSe_4$ to 2 $CuInSe_2$ were synthesized by Schorr *et al* [88]. For these $CuIn_x[Zn_{0.5}Sn_{0.5}]_{1-x}Se_2$ materials a miscibility gap in the region $0.4 < x < 0.8$ was found with a chalcopyrite crystal structure on the In-rich side of the gap and a kesterite structure on the (Zn,Sn)-rich side. Simultaneous Rietveld refinement of X-ray and neutron diffraction data revealed that mixing small amounts of $Cu_2ZnSnSe_4$ into $CuInSe_2$ leads to a random distribution of In, Zn and Sn atoms exclusively on the 4b position of the chalcopyrite structure, while mixing small amounts of $CuInSe_2$ into CZTSe influences all three cation sites in the kesterite structure.

Hartnauer *et al* were able to reproduce the reported miscibility gap with thin films prepared by co-evaporation [90]. Here, off-stoichiometric Cu-poor Zn-rich films with typical values of [Cu]/([Zn] + [Sn]) (CZT) and [Zn]/[Sn] (ZT) ratios of 0.7–0.8 and 1.3, respectively, were used. In this work, slightly increased

Figure 12. (left) Experimentally determined pseudo-ternary phase diagram of the CZTSe–CISe–ZnSe system for Cu-poor and Zn-rich CZTISe alloys. $I_{ZT} = [In] + ([Zn]-[Sn])/2 + 2[Sn]$ and $Z_E = ([Zn]-[Sn])/2$. Red lines on the edges: miscibility gaps between the two phases at the corners as determined in the literature. Black squares: *in situ* XRD confirmed single phased alloys. Red circles: phase-separated alloys. (right) Calculated Ehull (circles) and their interpolation (color map). Copyright © 2016, Author(s). Reproduced by [89]. CC BY 4.0.

efficiencies due to higher short circuit current densities were found for absorbers with small amounts of In, $([In]/([In] + [Zn] + [Sn])$ (IIZT) ratios of 0.07) were obtained. In pure, In-free and Zn rich co-evaporated CZTSe thin films with these ZT ratios, the presence of ZnSe secondary phases is commonly observed [90]. Interestingly, the addition of small amounts of In very effectively suppressed the segregation of this ZnSe secondary phase. In additional experiments, the absence of ZnSe segregation in the presence of moderate amounts of In was confirmed with XRD and Raman spectroscopy for absorbers with even higher ZT ratios of up to 1.83 [89]. The determined single and multi-phase regions within the 4 ZnSe- 2 CuInSe$_2$–CZTSe phase triangle at room temperature are summarized in figure 12, where stable compositions with single phase materials are marked with a black circle and compositions showing phase separation with a red circle. On the three sides of the triangle, regions with miscibility gaps according to literature data for the three pseudo-binary compositional variations between 4ZnSe–2CuInSe$_2$, 2CuInSe$_2$–CZTSe and CZTSe–4ZnSe are marked by red lines. The formation energies calculated with DFT support the experimental data and predict an enhanced stability for Zn-rich kesterites if small amounts of In are mixed into the CZTSe [89]. In figure 12, the thermodynamic stability as a result of these DFT calculations is given by E$_{Hull}$, the distance to the convex hull of stability, in a color-coded presentation for various points of the phase triangle. The smaller the E$_{Hull}$ (darker color), the more stable is the corresponding compound. According to these data, the introduction of small amounts of In into the CZTSe structure helps to accommodate larger amounts of Zn excess in the crystal structure and prevents the segregation of ZnSe secondary phases. Similar effects were found for the case of Ga [91].

In summary, In and Ga can be incorporated into the kesterite crystal structure in moderate amounts, without harming solar cell performance. In particular, the addition of In or Ga extends the potential of the kesterite structure to accommodate Zn excess without ZnSe segregation. For higher molar ratios of e.g. [2 CuInSe$_2$]/[CZTSe] > 0.4, phase separation is expected [92]. On the other hand, in the extreme case of completely Sn-free Cu-In-Zn-Se samples (upper-right edge of the phase triangle in figure 12) a broad solid-solution range of compounds with stoichiometries within the Cu(In,Ga)ZnSe$_3$-ZnSe pseudo-binary is found [93]. These alternative Sn-free, non-kesterite compounds exhibit a cubic zinc-blende structure and offer a tunable band gap from 1.1 eV (CuInZnSe$_3$) to 2.6 eV (ZnSe), rendering them suitable for photovoltaic applications [94].

5. Group IV

5.1. Silicon (Si)

At first glance, silicon is a very interesting element for alloying with the kesterite structure. Its abundance in the earth crust is by far higher than the other kesterite elements (282 000 ppm [95] or 28%) and the oxidation state +4 is very stable. Thus, it could be incorporated at the Sn-sites of the kesterite lattice and even prevent the instability that is related to the volatility of Sn and its tendency to be reduced to the +2 oxidation state [96]. Additionally, a band gap range of up to 2.4 eV [97] should be accessible for the Cu$_2$Zn(Si$_x$Sn$_{1-x}$)Se$_4$ alloy.

However, Cu$_2$ZnSiSe$_4$ has the wurtzstannite structure [98, 99] and there is a considerable size mismatch between Sn and Si [97]. Although first-principles calculations predicted miscibility in a wide compositional range [97], this could not be verified experimentally. In an evaporation-based study it was found, that Si does not

intermix with the kesterite lattice [100]. Only the Sn-free $Cu_2ZnSiSe_4$ could be formed, but the obtained photocurrent of complete devices was very low.

For $Cu_2Zn(Si_xSn_{1-x})S_4$ there is at least one report from Hamdi *et al* using a ceramic route that could form alloys up to x = 0.5 with a band gap of 1.7 eV that is ideal for an application in tandem solar cells [101]. However, no working solar cell devices have been demonstrated so far.

In addition to alloying it is worth to mention, that Si was also used in smaller quantities as a dopant for CZTSe absorbers and working solar cells were fabricated, but the efficiency was lower than for the reference and gradually decreases with the amount of Si [102].

In summary, Si can be incorporated into the kesterite lattice by substituting Sn. However, due to the high formation energy, the compounds are very challenging to synthesize. The solar cell efficiency clearly decreased with Si as a dopant and no working solar cells could be fabricated for the $Cu_2Zn(Si_xSn_{1-x})(S_ySe_{4-y})$ alloys.

5.2. Germanium (Ge)

Germanium (Ge) is probably one of the most suitable and interesting group IV elements for adding into the kesterite structure, in particular at the Sn-sites. Considering the most stable oxidation states of these two elements, +4 is more likely to occur with Ge than with Sn [103], thus avoiding presence of potentially harmful +2 oxidation states [104]. Additionally, a bandgap range from 1.0 to 2.25 eV is possible with the $Cu_2Zn(Sn_{1-x}Ge_x)(S_{1-y},Se_y)_4$ alloy [97, 105–107]. Several works can be found on the Ge addition in the kesterite host, from doping levels to alloying, including partial and total substitution of Sn, and some of them are here presented.

Regarding doping strategies, Giraldo *et al* reported the beneficial effect of Ge as dopant in CZTSe [108], observing a large efficiency improvement for very small quantities of Ge (<0.5% relative to Sn), followed by additional studies further exploring the origin/mechanisms involved in this approach [109–112]. Firstly, a strong impact on the morphology and grain size has been observed, frequently obtaining large grains [108, 112]. This was related to the formation of Ge-Se liquid phases (at ~380 °C) during the reactive annealing, acting as crystallization flux. Other beneficial effects of Ge have been reported, including interaction with Na with effect on the carriers concentration [111], modification of the reaction pathways minimizing Sn-Se phases formation (avoiding to a large extent the Sn loss and secondary phases formation) [112], passivation of detrimental grain boundaries related to high recombination [110], annihilation or minimization of Sn-related deep defects [113]. Through the optimization of doping strategies, by adding Ge nanolayers at the bottom and on top of metallic precursors, Ge doping has contributed to considerably reduce the V_{OC} deficit to <0.57 V thus achieving a record efficiency of 11.8% [112].

On the other hand, alloying approaches have been also investigated recently. As in the case of doping, Ge alloying of kesterite has immediately demonstrated a great potential, with device efficiencies ranging from 6.8 to 12.3% [114–122]. Among them, it is interesting to note that the best efficiency was achieved with a relative Ge content of 39% (i.e. (Ge/(Ge + Sn) = 0.39), through the optimization of a thermal annealing containing $GeSe_2$ [117, 119] leading to an improvement of the V_{OC} deficit by reducing band tailing, and a reduced carrier recombination at the absorber/buffer interface and/or in the space-charge region. Collord *et al* studied almost the full range of possible Ge/(Ge + Sn) compositional ratios (from 0 to 90%) by preparing a continuously graded sample with combinatorial mixing of Ge and Sn containing inks [118], and achieved an 11% efficiency solar cell with an optimized 25% Ge substitution (x = 0.25) with $E_g \sim 1.2$ eV), leading to a remarkable reduction of the V_{OC} deficit. Thus, the full range of Ge substitution has been investigated to some extent, including the pure Ge compound in recent reports, demonstrating that the CZGSe exhibits also kesterite structure [123]. Among the most relevant pure Ge kesterite results, Schnabel *et al* reported efficiencies exceeding 5% for a sulfo-selenide CZGSSe ($E_g \sim 1.5$ eV) solar cell [124], while for the selenide CZGSe (Eg ~ 1.4 eV) compound, Sahayaraj *et al* published a 5.5% efficiency device with a remarkable V_{OC} of 744 mV [125]. Intriguingly, the Ge based kesterite showed less electrical losses from band tailing/electrostatic potential fluctuations compared to Ge free devices [125, 126]. However, the main limiting factors were linked to a high series resistance, leading to imperfect current collection and a high interface recombination [127]. Trying to address these issues, a detailed optimization of the CdS chemical bath deposition has allowed achieving a record efficiency of 7.6% for a CZGSe ($E_g \sim 1.36$ eV) absorber [128].

6. Group V

6.1. Antimony (Sb)

In a large study assessing over 200 solar cells, Tiwari *et al* concluded that Sb and Na co-doping substantially improve the efficiency of Cu_2ZnSnS_4 (CZTS) prepared by thermolysis of molecular precursors as exemplified in figure 13(a) [129]. The introduction of Sb as a dopant was inspired by the positive effects on grain growth previously demonstrated in CIGS [130]. In the case of CZTS, Sb was also observed to act as a recrystallization flux leading to more effective grain growth and compact films as a result of a decrease in the enthalpy of I-4 phase formation [129]. Sb doping showed an overall improvement in key CZTS device metrics such as V_{OC} and fill
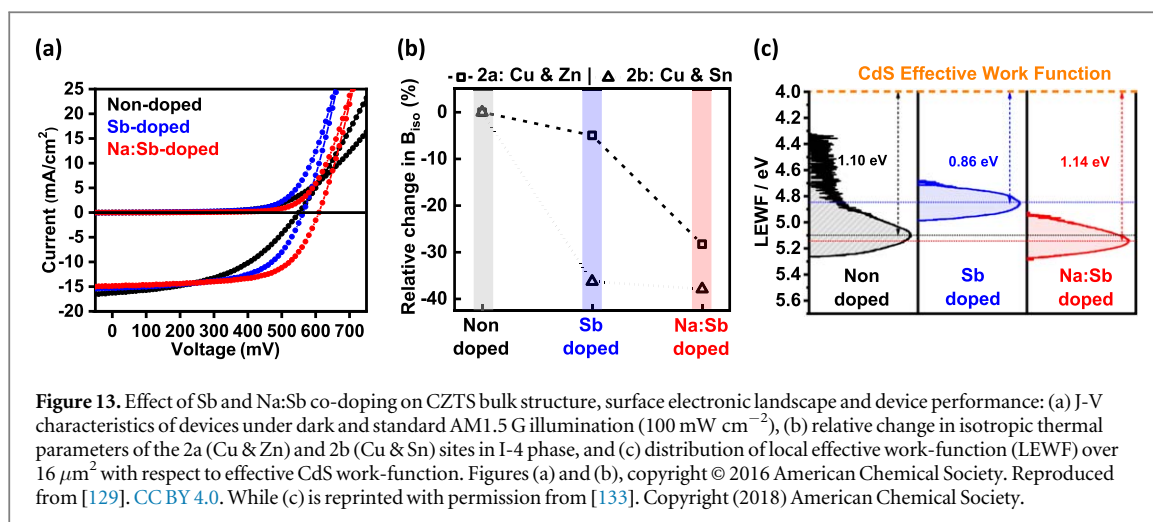
Figure 13. Effect of Sb and Na:Sb co-doping on CZTS bulk structure, surface electronic landscape and device performance: (a) J-V characteristics of devices under dark and standard AM1.5 G illumination (100 mW cm^{-2}), (b) relative change in isotropic thermal parameters of the 2a (Cu & Zn) and 2b (Cu & Sn) sites in I-4 phase, and (c) distribution of local effective work-function (LEWF) over 16 μm^2 with respect to effective CdS work-function. Figures (a) and (b), copyright © 2016 American Chemical Society. Reproduced from [129]. CC BY 4.0. While (c) is reprinted with permission from [133]. Copyright (2018) American Chemical Society.

factor, which comes as a result of a complex interplay of remediation of elemental disorder and improvement of band alignment. Figure 13(b) illustrates the decrease of the isotropic thermal parameter in Sn and Cu sites (as obtained by XRD structure refinement) upon Sb and Na doping, respectively, suggesting a significant decrease in disorder at these sites [129]. The effect of Sb on Sn disorder can be simply rationalized by their similar ionic radii (Sb, Z = 51 to Sn, Z = 50). Zhang *et al* showed by DFT Sb$_{Sn}$ exhibits smaller lattice relaxations and has lower formation energy than native CZTS defects [131]. It should be mentioned that Cu$_{Sn}$ and Zn$_{Sn}$ antisite domain boundaries have been experimentally observed by atomic resolution transmission electron microscopy in CZTS crystallites [132]. Furthermore, DFT supercell calculations by Chen *et al* concluded that such antisites give rise to mid-gap traps which could be highly detrimental to device performance [6].

Sb doping has also a strong effect on the surface electronic landscape of CZTS, as recently revealed by Tiwari *et al* using high-resolution energy-filtered photoelectron emission microscopy [133]. Figure 13(c) shows a substantial narrowing of the spatial distribution of effective work-function upon Sb and Na:Sb co-doping, which is another indication of a decreased elemental disorder. Sb (group V) generates donor states, which leads to a decrease of the overall work function, while Na co-doping result in a substantial work-function increase. Tiwari and co-workers also observed a grading of Sb content with a maximum concentration at the Mo/CZTS boundary of 0.069 ± 0.007 wt%, while Na co-doping led to 2.5 times lower Sb content [133]. Figure 13(c) also depicts how these trends can affect the CZTS/CdS barrier heights, which have shown a close correlation with recombination activation energies estimated by the temperature dependence of V_{OC} in devices [133]. Interestingly, this approximation to barrier heights enable estimating CZTSSe/CdS conduction band offsets in the range of 0.3 to 0.4 eV [134], which is consistent with values proposed in the literature [135]. However, quantitative analysis of band-offsets remains a highly challenging issue in view of elemental intermixing generated in high-quality junctions as exemplified by the elegant work by Bär *et al* [136].

7. Group VII-B and VIII-B

7.1. Manganese (Mn)
Among transition metal candidates, Mn is one of the promising elements to replace Zn. Electron configuration in Mn is quite stable at oxidation state +2, because of the nature of half-filled 3d^5-orbitals, instead of partially filled orbital in Fe, Ni or Co according to Pauli exclusion principles [137]. Furthermore, the cation radii mismatch in the 4-fold coordination between Mn^{2+} (0.80 Å) and Cu$^+$ (0.74 Å) is the largest compared to Zn^{2+} (0.74 Å), Fe^{2+} (0.77 Å), Co^{2+} (0.72 Å), and Ni^{2+} (0.69 Å) [18]. Based on DFT calculations, Cu$_2$MnSnS$_4$ (CMTS) should be thermodynamically stable in the stannite phase with I-42m space group symmetry [12] (see figure 14). In addition, Mn also has a higher relative abundance than Zn [138].

Most of the early studies of CMTS focused on investigating its magnetic, optical and electrical properties [139, 141, 142]. In terms of solar cell application, CMTS thin film is considered as absorber layer due to its similarly high absorption coefficient (>10^4 cm^{-1}) [142]. The direct band-gap of CMTS was calculated to be 1.52 eV which coincides with the measured 1.42–1.59 eV[143]. From reversible annealing treatments it was also concluded that just like CZTS disorder also occurs in CMTS.

Several studies have reported the photovoltaic performance of CMTSSe both for vacuum and non-vacuum based, even though the power conversion efficiency is generally rather poor (<1%) [144–148]. A highest conversion efficiency is 0.83% for CMTS solar cell with the ratio of Cu/(Mn + Sn) ≈0.8 and Mn/Sn ≈1.1

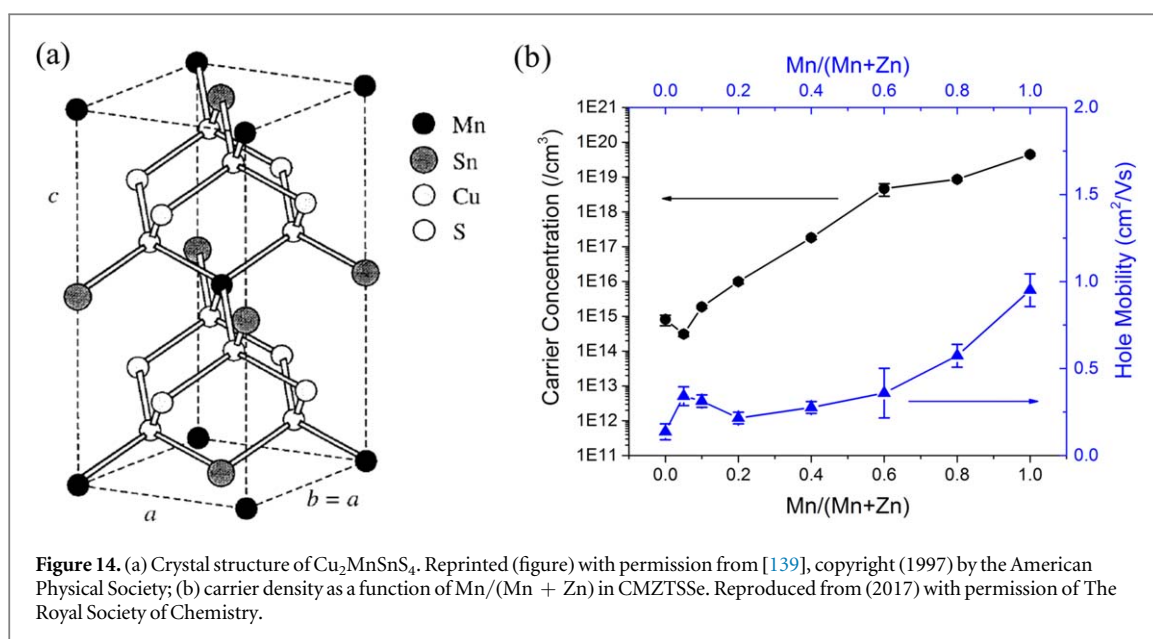**Figure 14.** (a) Crystal structure of Cu_2MnSnS_4. Reprinted (figure) with permission from [139], copyright (1997) by the American Physical Society; (b) carrier density as a function of Mn/(Mn + Zn) in CMZTSSe. Reproduced from (2017) with permission of The Royal Society of Chemistry.

synthesized through two-step thermal evaporation, while the record is 0.33% for CMTSSe by sol-gel technique [149]. One possible reason for the poor performance is due to the high carrier concentration ($\sim10^{19}$ cm^{-3}) [145].

In terms of partial substitution, $Cu_2Mn_xZn_{1-x}SnS_4$ (CMZTS) and $Cu_2Mn_xZn_{1-x}Sn(S,Se)_4$ (CMZTSSe) have been fabricated by different synthesis methods and shown improvement at low Mn substitution [150–153]. The highest solar cell efficiency is achieved at 5.7% for 15% Mn in CMZTS [150], and 8.9% for 5% Mn in CMZTSSe [151]. The enhancement is attributed to the improved grain growth, better interface between absorber and buffer, and a change in majority defects from Cu_{Zn} to V_{Cu} defects for CMZTSSe [150, 151]. As the amount of Mn substitution increases, the carrier concentration increased significantly (figure 14), and the radiative recombination is quenched, resulting in poor photovoltaic performance for samples with high Mn content [140].

7.2. Iron (Fe)

As a matter of fact, a natural mineral kesterite has formula $Cu_2(Zn,Fe)SnS_4$ [154] with an approximate content of Fe/(Fe + Zn) = 0.25. The quaternary chalcogenide Cu_2FeSnS_4 (CFTS) is commonly studied for its stability and the abundance and non-toxic nature of Fe. Unlike CZTS, CFTS is more stable in stannite crystal structure (ST) with an I-42m space group which shows less cationic disorder from the kesterite structure [155]. CFTS thin films have been fabricated by various methods, such as solvothermal [142], hot injection method [141], molecular method [156], spray pyrolysis [157], and mostly focused on its magnetic properties. Even though CFTS exhibit a band gap between 1–1.5 eV and high absorption coefficient (10^4 cm^{-1}) in the visible spectrum range [158], there are not many reported CFTS photovoltaic devices in literature. Efficiency of 0.07% is achieved with glass/Mo/CFTS/CdS/i-ZnO/AZO by using RF magnetron sputtering to deposit the absorber [159]. A. J. Pal group managed to synthesize CFTS with SILAR method and achieved solar cell efficiency of 2.95% by replacing the CdS buffer layer with the Bi_2S_3 buffer [160], which exhibits a more favorable band alignment at the interface as measured by scanning tunneling spectroscopy (STS) (figure 15). As pure CFTS has a high conductivity, it is also used as counter electrode in DSSC solar cell [157, 161]. Some usage in photoelectrochemical cells (PEC) [162] and n-type absorber in hybrid organic solar cell [163] have also been reported.

As for the Fe alloying in CZTS, both of Fe^{2+} (0.66 Å) and Zn^{2+} (0.64 Å) have similar ionic radii, which enables a solid solubility in the $Cu_2Zn_xFe_{1-x}SnS_4$ (CZFTS) [18]. There are few studies about CZFTS thin film properties which shows transformation from kesterite to stannite and increase in band gap (ranging from 1.35 eV to 1.7 eV) as the amount of Fe increases [156, 164–166]. However, a combinatorial study using spray coating showed a strong detrimental effect on quasi-Fermi level splitting (QLFS) in $Cu_2Zn_xFe_{1-x}Sn(S,Se)_4$ even at low concentrations of Fe [167]. So a possible positive role of Fe doping is doubtful as transition metals with a partially filled d-orbitals (Fe, Cr, Co) can introduce deep defect states within CZTSSe bandgap similarly to what is observed in CIGS absorbers [168, 169].

7.3. Nickel (Ni)

Another transition metal that can substitute for Zn is Ni since the ionic radius 0.69 Å for Ni^{2+} is close to 0.74 Å for Zn^{2+} [18]. Theoretical studies reported that the substitution of Ni for Zn in CZTS compound can potentially enhance

Figure 15. Schematic energy level diagram of CFTS/CdS, CFTS/Bi$_2$S$_3$, and CFTS/Ag$_2$S heterojunctions. The line at 0 V represents the Fermi energy after contact. Reprinted from [160]. Copyright (2017), with permission from Elsevier.
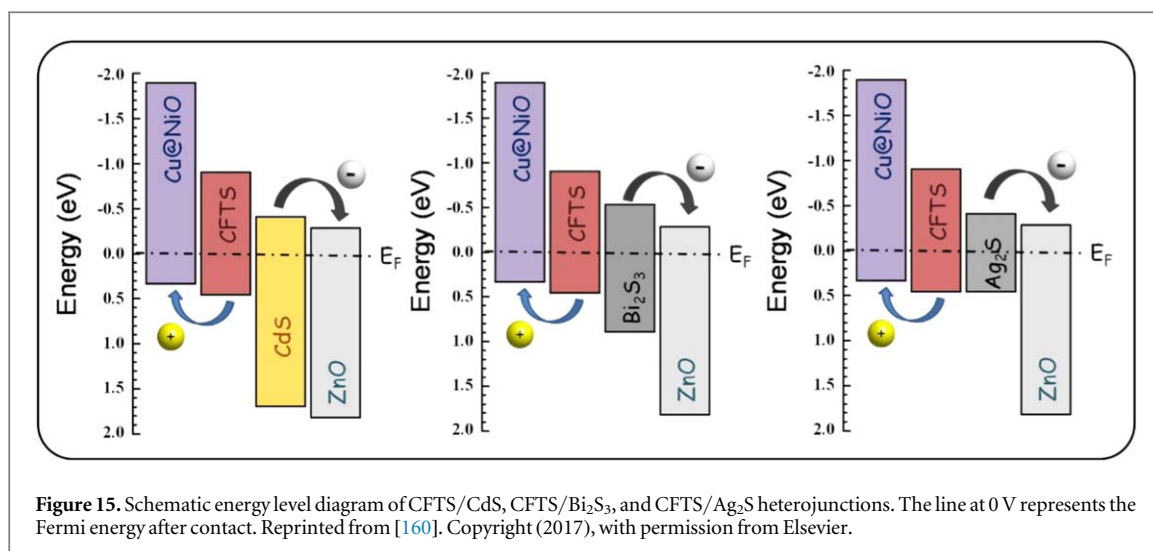
electrical conductivity and reduce the optical band gap [155]. However, the defects complex in Cu$_2$NiSnS$_4$ (CNTS) is predicted to yield localized in-gap states based on first principles density functional theory calculations [12].

Nevertheless, CNTS has been synthesized through various synthesis method such as hot-injection, solvothermal and hydrothermal to obtain nanoparticle CNTS [142, 170–174]. CNTS has an energy band gap of 1.5 ∼ 1.6 eV similar to CZTS and a high optical absorption coefficient of ∼10^6 cm^{-1} [142, 170–174]. CNTS exhibits the zincblende crystal structure while a complementary theoretical calculation predicts the P$\overline{4}$2c polytype as the most thermodynamically stable phase [175]. Two solar cell architectures with CNTS have been reported: a device architecture glass/Mo/CNTS/CdS/Al-ZnO/Al yielded 0.09% efficiency [175] whereas another structure utilizing ZnS coated on ZnO nanorods in the ITO/ZnO-nanorods/ZnS/CNTS/Au architecture yielded 2.71% [176]. It is not certain if the PV effect can be attributed to the CNTS absorber because comparable efficiencies were also obtained for Cu$_2$FeSnS$_4$ and Cu$_2$CoSnS$_4$ layers in the identical device structure.

8. Conclusions

8.1. What we learnt

The highest efficiency devices featuring extrinsic doping elements are summarized in tables 1 and 2, restricted to the one highest efficiency value per element (total area measurement whenever available). Without repeating dopant-specific results described in the previous sections, the following general observations can be deduced:

1. Several dopants have been reported to improve the performance of kesterite solar cells as compared to the nominally undoped reference devices. It is often difficult to differentiate between pure electronic effects of the dopant and other possible influences such as changes in the crystallization path leading to a different morphology, deviations in matrix composition, presence of alkali dopants coming from the substrates or atmosphere, etc.

2. Alkali dopants (Li, Na, K and to some extent Cs/Rb) have been proven to increase acceptor concentrations as well as to improve the morphology of the polycrystalline kesterite absorbers enabling more efficient devices. For the highest efficiency both matrix element composition and alkali dopant concentration must be carefully selected.

3. Alloying strategies by the isoelectronic substitution of Cu with Ag, Zn with Cd, or Sn with Ge do change the absorber bandgap as predicted within the solid solution ranges, can suppress the formation of secondary phases, and can partially reduce the disorder of the cation sub-lattice.

4. None of the reported doping or alloying strategies has succeeded in beating the record efficiency of the nominally 'undoped' device with 12.6% efficiency (which may contain Na-doping stemming from the glass substrate). This indicates that rather *intrinsic* defects are prevailing in kesterites, thus governing opto-electronic properties of the kesterite absorbers and providing an extraordinary tolerance against extrinsic doping.

Table 1. Compilation of the highest efficiency kesterite solar cells, which include extrinsic doping elements with concentration <1 mol%.

Material	Doping element	Eg (eV)	Voc (mV)	Eff (%, total area)	References
CZTSSe	nominally undoped[a]	1.13	513	12.6	[3]
CZTSSe	Li	1.04	449	11.5	[28]
CZTSe	Na	1.0	423	11.6	[42]
CZTSe	K	1.02	432	9.7	[48]
CZTSSe	Rb	0.96	419	8.8	[28]
CZTSSe	Cs	0.97	439	9.1	[28]
CZTSe	In	1.02	423	7.8	[87]
CZTSe	Ge	1.04	463	11.8[b]	[112]

[a] Unintentional Na doping from the glass substrate cannot be excluded.

[b] Active (illuminated area) measurement.

Table 2. Compilation of the highest efficiency kesterite solar cells which include extrinsic alloying elements with >1 mol%.

Material	Alloying element	Eg (eV)	VOC (mV)	Eff. (%, total area)	References
ACZTSSe	Ag/(Ag + Cu) = 3%	1.07	448	10.4	[61]
CMZTSSe	Mg/(Mg + Zn) = 4%	1.01	419	7.2	[76]
CZCTS	Cd/(Cd + Zn) = 40%	1.38	650	11.5	[79]
CZTGSe	Ge/(Ge + Sn) = 22%	1.11	527	12.3	[119]
CMZTS	Mn/(Mn + Zn) = 5%	1.055	418	8.9	[151]

8.2. What we need to learn

1. Research efforts to identify *intrinsic* defect(s) negatively affecting the minority carrier lifetime and diffusion length of the kesterite absorbers should be intensified. For instance, a recent theoretical study has suggested that the sulfur vacancy V_S that is stabilized by the presence of Sn^{2+} can act as a non-radiative site [104, 177]. This should be verified experimentally, and if confirmed, efforts can be targeted to test doping/alloying strategies that compensate these defects and stabilize the normal-valence oxidation state of Sn^{4+}.

2. When claiming the effectiveness of doping/alloying elements, high-efficiency reference (non-intentionally doped and/or alkali-doped) baseline samples with efficiencies > 8%–10% should preferably be used, otherwise the observed 'improvement' effect may erroneously be caused by a non-optimized baseline process.

3. Characterization techniques must be developed and widely used to reliably access important semiconductor absorber metrics such as the QFLS, defect concentration and their energetic position, carrier lifetime and diffusion length. This is important since common techniques such as TRPL do not yield reliable data on the minority carrier lifetime because some artefacts such as carrier trapping can affect measured PL decay times [10]. This will help to rapidly assess the optoelectronic properties of new compounds, thus assisting in search for new and effective doping/alloying strategies.

Acknowledgments

ORCID iDs

Yaroslav E Romanyuk ⦿ https://orcid.org/0000-0002-0529-228X
David J Fermin ⦿ https://orcid.org/0000-0002-0376-5506
Stener Lie ⦿ https://orcid.org/0000-0002-2601-8677
Lydia H Wong ⦿ https://orcid.org/0000-0001-9059-1745

References

[1] Lafond A, Choubrac L, Guillot-Deudon C, Deniard P and Jobic S 2012 Crystal structures of photovoltaic chalcogenides, an intricate puzzle to solve: the cases of CIGSe and CZTS *Materials Zeitschrift für Anorg. und Allg. Chemie* **638** 2571–7

[2] Gurieva G, Valle Rios L E, Franz A, Whitfield P and Schorr S 2018 Intrinsic point defects in off-stoichiometric $Cu_2ZnSnSe_4$: a neutron diffraction study *J. Appl. Phys.* **123** 161519

[3] Wang W, Winkler M T, Gunawan O, Gokmen T, Todorov T K, Zhu Y and Mitzi D B 2014 Device characteristics of CZTSSe thin-film solar cells with 12.6% efficiency *Adv. Energy Mater.* **4** 1301465

[4] Kim J *et al* 2014 High efficiency $Cu_2ZnSn(S,Se)_4$ solar cells by applying a double in 2 S 3/CdS emitter *Adv. Mater.* **26** 7427–31

[5] Katagiri H 2005 Cu_2ZnSnS_4 thin film solar cells *Thin Solid Films* **480–481** 426–32

[6] Chen S, Walsh A, Gong X-G and Wei S-H 2013 Classification of lattice defects in the kesterite Cu_2ZnSnS_4 and $Cu_2ZnSnSe_4$ Earth-abundant solar cell absorbers *Adv. Mater.* **25** 1522–39

[7] Shin D, Saparov B and Mitzi D B 2017 Defect engineering in multinary Earth-abundant chalcogenide photovoltaic materials *Adv. Energy Mater* **7** 1602366

[8] Kimerling L C 1974 Influence of deep traps on the measurement of free-carrier distributions in semiconductors by junction capacitance techniques *J. Appl. Phys.* **45** 1839–45

[9] Cwil M, Igalson M, Zabierowski P and Siebentritt S 2008 Charge and doping distributions by capacitance profiling in $Cu(In,Ga)Se_2$ solar cells *J. Appl. Phys.* **103** 063701

[10] Hages C J, Redinger A, Levcenko S, Hempel H, Koeper M J, Agrawal R, Greiner D, Kaufmann C A and Unold T 2017 Identifying the real minority carrier lifetime in nonideal semiconductors: a case study of kesterite *Materials Adv. Energy Mater* **7** 1–10

[11] Feurer T *et al* 2017 Progress in thin film CIGS photovoltaics - research and development, manufacturing, and applications *Prog. Photovoltaics Res. Appl.* **25** 645–67

[12] Chen R and Persson C 2017 Electronic and optical properties of Cu_2XSnS_4 (X = Be, Mg, Ca, Mn, Fe, and Ni) and the impact of native defect pairs *J. Appl. Phys.* **121** 203104

[13] Zhong G, Tse K, Zhang Y, Li X, Huang L, Yang C, Zhu J, Zeng Z, Zhang Z and Xiao X 2016 Induced effects by the substitution of Zn in Cu_2ZnSnX_4 (X = S and Se) *Thin Solid Films* **603** 224–9

[14] Tong Z *et al* 2019 Optical and photoelectrochemical properties of Cu_2SrSnS_4 thin film fabricated by a facial ball-milling method *Mater. Lett.* **237** 130–3

[15] Chen Z, Sun K, Su Z, Liu F, Tang D, Xiao H, Shi L, Jiang L, Hao X and Lai Y 2018 Solution-processed trigonal Cu_2BaSnS_4 thin-film solar cells *ACS Appl. Energy Mater.* **1** 3420–7

[16] Xiao Z, Meng W, Li J V and Yan Y 2017 Distant-atom mutation for better earth-abundant light absorbers: a case study of $Cu_2BaSnSe_4$ *ACS Energy Lett.* **2** 29–35

[17] Wei F and Zhi Z 2016 Quaternary sulphides $Cu_2Zn(Ti, Zr, Hf)S_4$, the new type of photovoltaic materials *Acta Phys. Sin.* **65** 1–13

[18] Shannon R D 1976 Revised effective ionic radii and systematic studies of interatomic distances in halides and chalcogenides *Acta Crystallogr. Sect. A* **32** 751–67

[19] Hallam B, Chen D, Kim M, Stefani B, Hoex B, Abbott M and Wenham S 2017 The role of hydrogenation and gettering in enhancing the efficiency of next-generation Si solar cells: an industrial perspective *Phys. Status Solidi* **214** 1700305

[20] Kılıç Ç and Zunger A 2003 N-type doping and passivation of $CuInSe_2$ and $CuGaSe_2$ by hydrogen *Phys. Rev. B* **68** 075201

[21] Otte K, Chassé T, Lippold G, Rauschenbach B and Szargan R 2002 Chemical defect explanation for the effect of postdeposition treatments on $CuInSe_2$ *J. Appl. Phys.* **91** 1624–7

[22] Park J *et al* 2018 The role of hydrogen from ALD-Al_2O_3 in kesterite Cu_2ZnSnS_4 solar cells: grain surface passivation *Adv. Energy Mater.* **8** 3–9

[23] Xin H, Vorpahl S M, Collord A D, Braly I L, Uhl A R, Krueger B W, Ginger D S and Hillhouse H W 2015 Lithium-doping inverts the nanoscale electric field at the grain boundaries in $Cu_2ZnSn(S,Se)_4$ and increases photovoltaic efficiency *Phys. Chem. Chem. Phys.* **17** 23859–66

[24] Yang Y, Kang X, Huang L and Pan D 2016 Tuning the band gap of $Cu_2ZnSn(S,Se)_4$ thin films via lithium alloying *ACS Appl. Mater. Interfaces* **8** 5308–13

[25] Lafond A, Guillot-Deudon C, Vidal J, Paris M, La C and Jobic S 2017 Substitution of Li for Cu in Cu_2ZnSnS_4: toward wide band gap absorbers with low cation disorder for thin film solar cells *Inorg. Chem.* **56** 2712–21

[26] Yang Y, Huang L and Pan D 2017 New insight of Li-doped $Cu_2ZnSn(S,Se)_4$ thin films: Li-induced Na diffusion from soda lime glass by a cation-exchange reaction *ACS Appl. Mater. Interfaces* **9** 23878–83

[27] Cabas-Vidani A *et al* 2018 High-efficiency $(Li_xCu_{1-x})_2ZnSn(S,Se)_4$ kesterite solar cells with lithium alloying *Adv. Energy Mater.* **8** 1801191

[28] Haass S G, Andres C, Figi R, Schreiner C, Bürki M, Romanyuk Y E and Tiwari A N 2018 Complex interplay between absorber composition and alkali doping in high-efficiency kesterite solar cells *Adv. Energy Mater.* **8** 1–9

[29] Mule A, Vermang B, Sylvester M, Brammertz G, Ranjbar S, Schnabel T, Gampa N, Meuris M and Poortmans J 2017 Effect of different alkali (Li, Na, K, Rb, Cs) metals on $Cu_2ZnSnSe_4$ solar cells *Thin Solid Films* **633** 156–61

[30] Maeda T, Kawabata A and Wada T 2015 First-principles study on alkali-metal effect of Li, Na, and K in Cu_2ZnSnS_4 and $Cu_2ZnSnSe_4$ *Phys. Status Solidi* **12** 631–7

[31] Altamura G, Wang M and Choy K-L 2016 Influence of alkali metals (Na, Li, Rb) on the performance of electrostatic spray-assisted vapor deposited $Cu_2ZnSn(S,Se)_4$ solar cells *Sci. Rep.* **6** 22109

[32] Hsieh Y-T, Han Q, Jiang C, Song T-B, Chen H, Meng L, Zhou H and Yang Y 2016 Efficiency enhancement of $Cu_2ZnSn(S,Se)_4$ solar cells via alkali metals doping *Adv. Energy Mater.* **6** 1502386

[33] Stolt L, Hedström J, Kessler J, Ruckh M, Velthaus K and Schock H 1993 ZnO/CdS/$CuInSe_2$ thin-film solar cells with improved performance *Appl. Phys. Lett.* **62** 597–9

[34] Repins I *et al* 2012 Co-evaporated $Cu_2ZnSnSe_4$ films and devices *Sol. Energy Mater. Sol. Cells* **101** 154–9

[35] Schnabel T, Abzieher T, Friedlmeier T M and Ahlswede E 2015 Solution-based preparation of $Cu_2ZnSn(S,Se)_4$ for solar cells—comparison of $SnSe_2$ and elemental se as chalcogen source *IEEE J. Photovoltaics* **5** 670–5

[36] Gershon T, Shin B, Bojarczuk N, Hopstaken M, Mitzi D B and Guha S 2015 The role of sodium as a surfactant and suppressor of non-radiative recombination at internal surfaces in Cu_2ZnSnS_4 *Adv. Energy Mater.* **5** 1400849

[37] Sutter-Fella C M, Stückelberger J A, Hagendorfer H, La Mattina F, Kranz L, Nishiwaki S, Uhl A R, Romanyuk Y E and Tiwari A N 2014 Sodium assisted sintering of chalcogenides and its application to solution processed $Cu_2ZnSn(S,Se)_4$ thin film solar cells *Chem. Mater.* **26** 1420–5

[38] Abzieher T, Schnabel T, Hetterich M, Powalla M and Ahlswede E 2016 Source and effects of sodium in solution-processed kesterite solar cells *Phys. Status Solidi* **213** 1039–49

[39] Andres C *et al* 2018 Decoupling of optoelectronic properties from morphological changes in sodium treated kesterite thin film solar cells *Sol. Energy* **175** 94–100

[40] Werner M, Sutter-Fella C M, Romanyuk Y E and Tiwari A N 2015 8.3% efficient $Cu_2ZnSn(S,Se)_4$ solar cells processed from sodium-containing solution precursors in a closed reactor *Thin Solid Films* **582** 308–12

[41] Haass S G, Diethelm M, Werner M, Bissig B, Romanyuk Y E and Tiwari A N 2015 11.2% efficient solution processed kesterite solar cell with a low voltage deficit *Adv. Energy Mater.* **5** 1–7

[42] Lee Y S, Gershon T, Gunawan O, Todorov T K, Gokmen T, Virgus Y and Guha S 2015 $Cu_2ZnSnSe_4$ thin-film solar cells by thermal Co-evaporation with 11.6% efficiency and improved minority carrier diffusion length *Adv. Energy Mater.* **5** 1401372

[43] Schwarz T, Cojocaru-Mirédin O, Choi P, Mousel M, Redinger A, Siebentritt S and Raabe D 2015 Atom probe tomography study of internal interfaces in $Cu_2ZnSnSe_4$ thin-films *J. Appl. Phys.* **118** 095302

[44] Cojocaru-Mirédin O, Choi P-P, Abou-Ras D, Schmidt S S, Caballero R and Raabe D 2011 Characterization of grain boundaries in $Cu(In,Ga)Se_2$ films using atom-probe tomography *IEEE J. Photovoltaics* **1** 207–12

[45] Tong Z, Yan C, Su Z, Zeng F, Yang J, Li Y, Jiang L, Lai Y and Liu F 2014 Effects of potassium doping on solution processed kesterite Cu_2ZnSnS_4 thin film solar cells *Appl. Phys. Lett.* **105** 223903

[46] Li W, Su Z, Tan J M R, Chiam S Y, Seng H L, Magdassi S and Wong L H 2017 Revealing the role of potassium treatment in CZTSSe thin film solar cells *Chem. Mater.* **29** 4273–81

[47] Haass S G, Diethelm M, Andres C, Romanyuk Y E and Tiwari A N 2017 Potassium post deposition treatment of solution-processed kesterite solar cells *Thin Solid Films* **633** 131–4

[48] Haass S G, Andres C, Figi R, Schreiner C, Bürki M, Tiwari A N and Romanyuk Y E 2018 Effects of potassium on kesterite solar cells: Similarities, differences and synergies with sodium *AIP Adv.* **8** 015133

[49] López-Marino S *et al* 2016 Alkali doping strategies for flexible and light-weight $Cu_2ZnSnSe_4$ solar cells *J. Mater. Chem.* A **4** 1895–907

[50] Reinhard P *et al* 2015 Features of KF and NaF postdeposition treatments of $Cu(In,Ga)Se_2$ absorbers for high efficiency thin film solar cells *Chem. Mater.* **27** 5755–64

[51] Cadel E, Barreau N, Kessler J and Pareige P 2010 Atom probe study of sodium distribution in polycrystalline $Cu(In,Ga)Se_2$ thin film *Acta Mater.* **58** 2634–7

[52] Sangster J and Pelton A D 1997 The Na-Se (Sodium-Selenium) System *J. Phase Equilibria* **18** 185–9

[53] Sangster J and Pelton A D 1997 The K-Se (Potassium-Selenium) System *J. Phase Equilibria* **18** 177–80

[54] Sangster J and Pelton A D 1997 The Li-Se (Lithium-Selenium) System *J. Phase Equilibria* **18** 181–4

[55] Sangster J and Pelton A D 1997 The Cs-Se(Cesium-Selenium)system *J. Phase Equilibria* **18** 173–6

[56] Sangster J and Pelton A D 1997 The Rb-Se (Rubidium-Selenium) System *J. Phase Equilibria* **18** 190–3

[57] Haass S G 2017 Alkali treatment of solution processed kesterite solar cells *PhD Thesis*, ETH Zürich https://doi.org/10.3929/ethz-b-000235925

[58] Gershon T, Lee Y S, Antunez P, Mankad R, Singh S, Bishop D, Gunawan O, Hopstaken M and Haight R 2016 Photovoltaic materials and devices based on the alloyed kesterite absorber $(Ag_xCu_{1-x})_2ZnSnSe_4$ *Adv. Energy Mater.* **6** 1502468

[59] Guchhait A, Su Z, Tay Y F, Shukla S, Li W, Leow S W, Tan J M R, Lie S, Gunawan O and Wong L H 2016 Enhancement of open-circuit voltage of solution-processed Cu_2ZnSnS_4 solar cells with 7.2% efficiency by incorporation of silver *ACS Energy Lett.* **1** 1256–61

[60] Hages C J, Koeper M J and Agrawal R 2016 Optoelectronic and material properties of nanocrystal-based CZTSe absorbers with Ag-alloying *Sol. Energy Mater. Sol. Cells* **145** 342–8

[61] Qi Y, Tian Q, Meng Y, Kou D, Zhou Z, Zhou W and Wu S 2017 Elemental precursor solution processed $(Cu_{1-x}Ag_x)_2ZnSn(S,Se)_4$ photovoltaic devices with over 10% efficiency *ACS Appl. Mater. Interfaces* **9** 21243–50

[62] Qi Y-F, Kou D-X, Zhou W-H, Zhou Z-J, Tian Q-W, Meng Y-N, Liu X-S, Du Z-L and Wu S-X 2017 Engineering of interface band bending and defects elimination via a Ag-graded active layer for efficient $(Cu,Ag)_2ZnSn(S,Se)_4$ solar cells *Energy Environ. Sci.* **10** 2401–10

[63] Bourdais S *et al* 2016 Is the Cu/Zn disorder the main culprit for the voltage deficit in kesterite solar cells? *Adv. Energy Mater.* **6** 1502276

[64] Wang C, Chen S, Yang J-H, Lang L, Xiang H-J, Gong X-G, Walsh A and Wei S-H 2014 Design of I2–II–IV–VI4 semiconductors through element substitution: the thermodynamic stability limit and chemical trend *Chem. Mater.* **26** 3411–7

[65] Yuan Z-K, Chen S, Xiang H, Gong X-G, Walsh A, Park J-S, Repins I and Wei S-H 2015 Engineering solar cell absorbers by exploring the band alignment and defect disparity: the case of Cu- and Ag-based kesterite compounds *Adv. Funct. Mater.* **25** 6733–43

[66] Cherns D, Griffiths I J, Jones L, Bishop D M, Lloyd M A and McCandless B E 2018 Direct observation of high densities of antisite defects in $Ag_2ZnSnSe_4$ *ACS Appl. Energy Mater.* **1** 6260–7

[67] Zhu T, Huhn W P, Wessler G C, Shin D, Saparov B, Mitzi D B and Blum V 2017 I2–II–IV–VI4 (I = Cu, Ag; II = Sr, Ba; IV = Ge, Sn; VI = S, Se): chalcogenides for thin-film photovoltaics *Chem. Mater.* **29** 7868–79

[68] Sai Gautam G, Senftle T P and Carter E A 2018 Understanding the effects of Cd and Ag doping in Cu_2ZnSnS_4 solar cells *Chem. Mater.* **30** 4543–55

[69] Gong W, Tabata T, Takei K, Morihama M, Maeda T and Wada T 2015 Crystallographic and optical properties of $(Cu, Ag)_2ZnSnS_4$ and $(Cu,Ag)_2ZnSnSe_4$ solid solutions *Phys. Status Solidi* **12** 700–3

[70] Gurieva G, Franz A, Prieto J M, Unold T and Schorr S 2018 Structural and optoelectronic characterization of $(Ag_xCu_{1-x})ZnSnSe_4$ solid solution *2018 IEEE 7th World Conf. on Photovoltaic Energy Conversion (WCPEC) A Joint Conf. of 45th IEEE PVSC (Piscataway, NJ)* (IEEE) pp 0808–11

[71] Gershon T, Sardashti K, Gunawan O, Mankad R, Singh S, Lee Y S, Ott J A, Kummel A and Haight R 2016 Photovoltaic device with over 5% efficiency based on an n-type $Ag_2ZnSnSe_4$ absorber *Adv. Energy Mater.* **6** 1601182

[72] Hadke S H, Levcenko S, Lie S, Hages C J, Márquez J A, Unold T and Wong L H 2018 Synergistic effects of double cation substitution in solution-processed CZTS solar cells with over 10% efficiency *Adv. Energy Mater.* **8** 1802540

[73] Nguyen T H, Kawaguchi T, Chantana J, Minemoto T, Harada T, Nakanishi S and Ikeda S 2018 Structural and solar cell properties of a Ag-containing Cu_2ZnSnS_4 thin film derived from spray pyrolysis *ACS Appl. Mater. Interfaces* **10** 5455–63

[74] Guo Y, Cheng W, Jiang J, Zuo S, Shi F and Chu J 2016 The structural, morphological and optical–electrical characteristic of $Cu2XSnS4$ (X:Cu,Mg) thin films fabricated by novel ultrasonic co-spray pyrolysis *Mater. Lett.* **172** 68–71

[75] Kuo D-H and Wubet W 2014 Mg dopant in $Cu_2ZnSnSe_4$: an n-type former and a promoter of electrical mobility up to 120 cm^2 V^{-1} s^{-1} *J. Solid State Chem.* **215** 122–7

[76] Caballero R, Haass S G, Andres C, Arques L, Oliva F, Izquierdo-Roca V and Romanyuk Y E 2018 Effect of magnesium incorporation on solution-processed kesterite solar cells *Front. Chem.* **6** 1–9

[77] Slater J C 1964 Atomic radii in crystals *J. Chem. Phys.* **41** 3199–204

[78] Su Z, Tan J M R, Li X, Zeng X, Batabyal S K and Wong L H 2015 Cation substitution of solution-processed Cu_2ZnSnS_4 thin film solar cell with over 9% efficiency *Adv. Energy Mater.* **5** 2–8

[79] Yan C *et al* 2017 Beyond 11% efficient sulfide kesterite $Cu_2Zn_xCd_{1-x}SnS_4$ solar cell: effects of cadmium alloying *ACS Energy Lett.* **2** 930–6

[80] Pilvet M, Kauk-Kuusik M, Altosaar M, Grossberg M, Danilson M, Timmo K, Mere A and Mikli V 2015 Compositionally tunable structure and optical properties of $Cu_{1.85}(Cd_xZn_{1-x})_{1.1} SnS_{4.1}(0 \leqslant x \leqslant 1)$ monograin powders *Thin Solid Films* **582** 180–3

[81] Fu J, Tian Q, Zhou Z, Kou D, Meng Y, Zhou W and Wu S 2016 Improving the performance of solution-processed $Cu_2ZnSn(S,Se)_4$ photovoltaic materials by Cd^{2+} substitution *Chem. Mater.* **28** 5821–8

[82] Duan H-S, Yang W, Bob B, Hsu C-J, Lei B and Yang Y 2013 The role of sulfur in solution-processed $Cu_2ZnSn(S,Se)_4$ and its effect on defect properties *Adv. Funct. Mater.* **23** 1466–71

[83] Wu S-H, Chang C-W, Chen H-J, Shih C-F, Wang Y-Y, Li C-C and Chan S-W 2017 High-efficiency $Cu_2ZnSn(S,Se)_4$ solar cells fabricated through a low-cost solution process and a two-step heat treatment *Prog. Photovoltaics Res. Appl.* **25** 58–66

[84] Li J, Kim S, Nam D, Liu X, Kim J, Cheong H, Liu W, Li H, Sun Y and Zhang Y 2017 Tailoring the defects and carrier density for beyond 10% efficient CZTSe thin film solar cells *Sol. Energy Mater. Sol. Cells* **159** 447–55

[85] Sun R, Zhuang D, Zhao M, Gong Q, Scarpulla M, Wei Y, Ren G and Wu Y 2018 Beyond 11% efficient $Cu_2ZnSn(Se,S)_4$ thin film solar cells by cadmium alloying *Sol. Energy Mater. Sol. Cells* **174** 494–8

[86] Yan C *et al* 2018 Cu_2ZnSnS_4 solar cells with over 10% power conversion efficiency enabled by heterojunction heat treatment *Nat. Energy* **3** 764–72

[87] Giraldo S, Ruiz C M, Espíndola-Rodríguez M, Sánchez Y, Placidi M, Cozza D, Barakel D, Escoubas L, Pérez-Rodríguez A and Saucedo E 2016 Optical and electrical properties of In-doped $Cu_2ZnSnSe_4$ *Sol. Energy Mater. Sol. Cells* **151** 44–51

[88] Schorr S, Tovar M, Hoebler H-J and Schock H-W 2009 Structure and phase relations in the $2(CuInS_2)–Cu_2ZnSnS_4$ solid solution system *Thin Solid Films* **517** 2508–10

[89] Hartnauer S, Körbel S, Marques M A L, Botti S, Pistor P and Scheer R 2016 Research Update: Stable single-phase Zn-rich $Cu_2ZnSnSe_4$ through In doping *APL Mater.* **4** 070701

[90] Hartnauer S 2016 Phasenbildung am system Cu-Zn-Sn-(In,Ga)-S-Se untersucht mit echtzeitmethoden für chalkogenid-dünnschichtsolarzellen *PhD Thesis*, Martin-Luther-Universität Halle-Wittenberg http://digital.bibliothek.uni-halle.de/ulbhalhs/urn/urn:nbn:de:gbv:3:4-19326

[91] Hartnauer S 2016 *Phasenbildung am System Cu-Zn-Sn-(In,Ga)-S-Se untersucht mit Echtzeitmethoden für Chalkogenid-Dünnschichtsolarzellen* (Martin-Luther-Universität Halle-Wittenberg)

[92] Schorr S 2007 Structural aspects of adamantine like multinary chalcogenides *Thin Solid Films* **515** 5985–91

[93] Schorr S, Riede V, Spemann D and Doering T 2006 Electronic band gap of $Zn_2x(CuIn)_{1-x}X_2$ solid solution series (X = S, Se, Te) *J. Alloys Compd.* **414** 26–30

[94] Kondrotas R, Oliva F, Alcobe X, Izquierdo-Roca V, Perez-Rodriguez A, Saucedo E and Pistor P 2018 Double band gap gradients in sequentially processed photovoltaic absorbers from the $Cu(In,Ga)Se_2-ZnSe$ pseudobinary system *Prog. Photovoltaics Res. Appl.* **26** 135–44

[95] Grazman B 1991 *Handbook of Chemistry and Physics* 71st edn, ed D R Lide (Boca Raton, FL: CRC Press)

[96] Redinger A, Berg D M, Dale P J and Siebentritt S 2011 The consequences of kesterite equilibria for efficient solar cells *J. Am. Chem. Soc.* **133** 3320–3

[97] Shu Q, Yang J-H, Chen S, Huang B, Xiang H, Gong X-G and Wei S-H 2013 $Cu_2Zn(Sn,Ge)Se_4$ and $Cu_2Zn(Sn,Si)Se_4$ alloys as photovoltaic materials: Structural and electronic properties *Phys. Rev. B* **87** 115208

[98] Litvinchuk A P, Dzhagan V M, Yukhymchuk V O, Valakh M Y, Parasyuk O V, Piskach L V, Wang X, Jacobson A J and Zahn D R T 2016 Crystal structure and vibrational properties of $Cu2ZnSiSe4$ quaternary semiconductor *Phys. Status Solidi* **253** 1808–15

[99] Gurieva G, Levcenko S, Kravtsov V C, Nateprov A, Irran E, Huang Y-S, Arushanov E and Schorr S 2015 X-ray diffraction investigation on $Cu_2ZnSiSe_4$ single and polycrystalline crystals *Zeitschrift für Krist.—Cryst. Mater.* **230**

[100] Brammertz G, Vermang B, ElAnzeery H, Sahayaraj S, Ranjbar S, Meuris M and Poortmans J 2017 Fabrication of ternary and quaternary chalcogenide compounds based on Cu, Zn, Sn and Si for thin film photovoltaic applications *Phys. Status Solidi Curr. Top. Solid State Phys.* **14** 1600162

[101] Hamdi M, Lafond A, Guillot-Deudon C, Hlel F, Gargouri M and Jobic S 2014 Crystal chemistry and optical investigations of the $Cu_2Zn(Sn,Si)S_4$ series for photovoltaic applications *J. Solid State Chem.* **220** 232–7

[102] Giraldo S, Neuschitzer M, Izquierdo-Roca V, Perez-Rodriguez A and Saucedo E 2018 Doping effects on kesterites other than alkalis *2018 IEEE 7th World Conf. on Photovoltaic Energy Conversion (WCPEC) A Joint Conf. of 45th IEEE PVSC (Piscataway, NJ)* (IEEE) pp 3869–72 28th PVSEC & 34th EU PVSEC

[103] Earnshaw A and Greenwood N 1997 *Chemistry of the Elements* 2nd edn (Oxford: Elsevier, Butterworth-Heinemann)

[104] Kim S, Park J-S, Hood S N and Walsh A 2019 Lone-pair effect on carrier capture in Cu_2ZnSnS_4 solar cells *J. Mater. Chem.* A **7** 2686–93

[105] Grossberg M, Timmo K, Raadik T, Kärber E, Mikli V and Krustok J 2015 Study of structural and optoelectronic properties of $Cu_2Zn(Sn_{1−x}Ge_x)Se_4$ ($x = 0$ to 1) alloy compounds *Thin Solid Films* **582** 176–9

[106] Khadka D B and Kim J 2015 Band gap engineering of alloyed $Cu_2ZnGe_xSn_{1−x}Q_4$ (Q = S,Se) Films for Solar Cell *J. Phys. Chem.* C **119** 1706–13

[107] Garcia-Llamas E, Merino J M, Serna R, Fontané X, Victorov I A, Pérez-Rodríguez A, León M, Bodnar I V, Izquierdo-Roca V and Caballero R 2016 Wide band-gap tuning $Cu_2ZnSn_{1−x}GeS_4$ single crystals: optical and vibrational properties *Sol. Energy Mater. Sol. Cells* **158** 147–53

[108] Giraldo S *et al* 2015 Large efficiency improvement in $Cu_2ZnSnSe_4$ solar cells by introducing a superficial Ge nanolayer *Adv. Energy Mater.* **5** 1–6

[109] Giraldo S, Thersleff T, Larramona G, Neuschitzer M, Pistor P, Leifer K, Pérez-Rodríguez A, Moisan C, Dennler G and Saucedo E 2016 $Cu_2ZnSnSe_4$ solar cells with 10.6% efficiency through innovative absorber engineering with Ge superficial nanolayer *Prog. Photovoltaics Res. Appl.* **24** 1359–67

[110] Thersleff T, Giraldo S, Neuschitzer M, Pistor P, Saucedo E and Leifer K 2017 Chemically and morphologically distinct grain boundaries in Ge-doped $Cu_2ZnSnSe_4$ solar cells revealed with STEM-EELS *Mater. Des.* **122** 102–9

[111] Giraldo S, Neuschitzer M, Placidi M, Pistor P, Perez-Rodriguez A and Saucedo E 2016 $Cu_2ZnSnSe_4$ -based solar cells with efficiency exceeding 10% by adding a superficial Ge nanolayer: the interaction between Ge and Na *IEEE J. Photovoltaics* **6** 754–9

[112] Giraldo S *et al* 2018 How small amounts of Ge modify the formation pathways and crystallization of kesterites *Energy Environ. Sci.* **11** 582–93

[113] Neuschitzer M, Rodriguez M E, Guc M, Marquez J A, Giraldo S, Forbes I, Perez-Rodriguez A and Saucedo E 2018 Revealing the beneficial effects of Ge doping on $Cu_2ZnSnSe_4$ thin film solar cells *J. Mater. Chem.* A **6** 11759–72

[114] Ford G M, Guo Q, Agrawal R and Hillhouse H W 2011 Earth abundant element $Cu_2Zn(Sn_{1−x}Gex)S_4$ nanocrystals for tunable band gap solar cells: 6.8% efficient device fabrication *Chem. Mater.* **23** 2626–9

[115] Guo Q, Ford G M, Yang W-C, Hages C J, Hillhouse H W and Agrawal R 2012 Enhancing the performance of CZTSSe solar cells with Ge alloying *Sol. Energy Mater. Sol. Cells* **105** 132–6

[116] Hages C J, Levcenco S, Miskin C K, Alsmeier J H, Abou-Ras D, Wilks R G, Bär M, Unold T and Agrawal R 2015 Improved performance of Ge-alloyed CZTGeSSe thin-film solar cells through control of elemental losses *Prog. Photovoltaics Res. Appl.* **23** 376–84

[117] Kim S, Kim K M, Tampo H, Shibata H, Matsubara K and Niki S 2016 Ge-incorporated $Cu_2ZnSnSe_4$ thin-film solar cells with efficiency greater than 10% *Sol. Energy Mater. Sol. Cells* **144** 488–92

[118] Collord A D and Hillhouse H W 2016 Germanium alloyed kesterite solar cells with low voltage deficits *Chem. Mater.* **28** 2067–73

[119] Kim S, Kim K M, Tampo H, Shibata H and Niki S 2016 Improvement of voltage deficit of Ge-incorporated kesterite solar cell with 12.3% conversion efficiency *Appl. Phys. Express* **9** 102301

[120] Khadka D B, Kim S and Kim J 2016 Effects of Ge alloying on device characteristics of kesterite-based CZTSSe thin film solar cells *J. Phys. Chem.* C **120** 4251–8

[121] Márquez J *et al* 2017 Chemistry and dynamics of Ge in kesterite: toward band-gap-graded absorbers *Chem. Mater.* **29** 9399–406

[122] Andres C, Cabas-Vidani A, Tiwari A N and Romanyuk Y E 2018 From sputtered metal precursors towards $Cu_2Zn(Sn_{1-x},Ge_x)Se_4$ thin film solar cells with shallow back grading *Thin Solid Films* **665** 168–72

[123] Gunder R, Márquez-Prieto J A, Gurieva G, Unold T and Schorr S 2018 Structural characterization of off-stoichiometric kesterite-type $Cu_2ZnGeSe_4$ compound semiconductors: from cation distribution to intrinsic point defect density *Cryst. Eng. Comm.* **20** 1491–8

[124] Schnabel T, Seboui M and Ahlswede E 2017 Evaluation of different metal salt solutions for the preparation of solar cells with wide-gap $Cu_2ZnGeS_xSe_{4−x}$ absorbers *RSC Adv.* **7** 26–30

[125] Sahayaraj S, Brammertz G, Vermang B, Schnabel T, Ahlswede E, Huang Z, Ranjbar S, Meuris M, Vleugels J and Poortmans J 2017 Optoelectronic properties of thin film $Cu_2ZnGeSe_4$ solar cells *Sol. Energy Mater. Sol. Cells* **171** 136–41

[126] Nagaya K, Fujimoto S, Tampo H, Kim S, Nishiwaki M, Nishigaki Y, Kato M, Shibata H and Fujiwara H 2018 Very small tail state formation in $Cu_2ZnGeSe_4$ *Appl. Phys. Lett.* **113** 093901

[127] Oueslati S, Grossberg M, Kauk-Kuusik M, Mikli V, Ernits K, Meissner D and Krustok J 2019 Effect of germanium incorporation on the properties of kesterite $Cu_2ZnSn(S,Se)_4$ monograins *Thin Solid Films* **669** 315–20

[128] Choubrac L, Brammertz G, Barreau N, Arzel L, Harel S, Meuris M and Vermang B 2018 7.6% CZGSe solar cells thanks to optimized CdS chemical bath deposition *Phys. Status Solidi* **215** 1800043

[129] Tiwari D, Koehler T, Lin X, Harniman R, Griffiths I, Wang L, Cherns D, Klenk R and Fermin D J 2016 Cu_2ZnSnS_4 thin films generated from a single solution based precursor: the effect of Na and Sb doping *Chem. Mater.* **28** 4991–7

[130] Yuan M, Mitzi D B, Liu W, Kellock A J, Chey S J and Deline V R 2010 Optimization of CIGS-based PV device through antimony doping *Chem. Mater.* **22** 285–7

[131] Zhang X, Han M, Zeng Z and Duan Y 2017 The role of Sb in solar cell material Cu_2ZnSnS_4 *J. Mater. Chem.* A **5** 6606–12

[132] Kattan N A, Griffiths I J, Cherns D and Fermín D J 2016 Observation of antisite domain boundaries in Cu_2ZnSnS_4 by atomic-resolution transmission electron microscopy *Nanoscale* **8** 14369–73

[133] Tiwari D, Cattelan M, Harniman R L, Sarua A, Fox N, Koehler T, Klenk R and Fermin D J 2018 Impact of Sb and Na doping on the surface electronic landscape of Cu_2ZnSnS_4 thin films *ACS Energy Lett.* **3** 2977–82

[134] Tiwari D, Cattelan M, Harniman R L, Sarua A, Abbas A, Bowers J W, Fox N A and Fermin D J 2018 Mapping shunting paths at the surface of $Cu_2ZnSn(S,Se)_4$ films via energy-filtered photoemission microscopy *iScience* **9** 36–46

[135] Crovetto A and Hansen O 2017 What is the band alignment of $Cu_2ZnSn(S,Se)_4$ solar cells ? *Sol. Energy Mater. Sol. Cells* **169** 177–94

[136] Bär M, Repins I, Weinhardt L, Alsmeier J-H, Pookpanratana S, Blum M, Yang W, Heske C, Wilks R G and Noufi R 2017 Zn–Se–Cd–S interlayer formation at the CdS/$Cu_2ZnSnSe_4$ thin-film solar cell interface *ACS Energy Lett.* **2** 1632–40

[137] Housecroft C E and Sharpe A G 2012 *Inorganic Chemistry* 4th edn (Harlow: Pearson)

[138] Unold T and Schock H W 2011 Nonconventional (Non-Silicon-Based) photovoltaic materials *Annu. Rev. Mater. Res.* **41** 297–321

[139] Fries T, Shapira Y, Palacio F, Morón M C, McIntyre G J, Kershaw R, Wold A and McNiff E J 1997 Magnetic ordering of the antiferromagnet Cu_2MnSnS_4 from magnetization and neutron-scattering measurements *Phys. Rev.* B **56** 5424–31

[140] Lie S, Rui Tan J M, Li W, Leow S W, Tay Y F, Bishop D M, Gunawan O and Wong L H 2018 Reducing the interfacial defect density of CZTSSe solar cells by Mn substitution *J. Mater. Chem.* A **6** 1540–50

[141] Liang X, Guo P, Wang G, Deng R, Pan D and Wei X 2012 Dilute magnetic semiconductor Cu2MnSnS4 nanocrystals with a novel zincblende and wurtzite structure *RSC Adv.* **2** 5044

[142] Cui Y, Deng R, Wang G and Pan D 2012 A general strategy for synthesis of quaternary semiconductor Cu_2MSnS_4 (M = Co^{2+}, Fe^{2+}, Ni^{2+}, Mn^{2+}) nanocrystals *J. Mater. Chem.* **22** 23136

[143] Rudisch K, Espinosa-García W F, Osorio-Guillén J M, Araujo C M, Platzer-Björkman C and Scragg J J S 2019 Structural and electronic properties of Cu₂MnSnS₄ from experiment and first-principles calculations *Phys. Status Solidi* **256** 1800743

[144] Marchionna S, Le Donne A, Merlini M, Binetti S, Acciarri M and Cernuschi F 2017 Growth of Cu₂MnSnS₄ PV absorbers by sulfurization of evaporated precursors *J. Alloys Compd.* **693** 95–102

[145] Prabhakar R R, Zhenghua S, Xin Z, Baikie T, Woei L S, Shukla S, Batabyal S K, Gunawan O and Wong L H 2016 Photovoltaic effect in earth abundant solution processed Cu₂MnSnS₄ and Cu MnSn(S,Se)₄ thin films *Sol. Energy Mater. Sol. Cells* **157** 867–73

[146] Le Donne A, Marchionna S, Acciarri M, Cernuschi F and Binetti S 2017 Relevant efficiency enhancement of emerging Cu₂MnSnS₄ thin film solar cells by low temperature annealing *Sol. Energy* **149** 125–31

[147] Chen L, Deng H, Tao J, Cao H, Huang L, Sun L, Yang P and Chu J 2015 Synthesis and characterization of earth-abundant Cu₂MnSnS₄ thin films using a non-toxic solution-based technique *RSC Adv.* **5** 84295–302

[148] Yu J, Deng H, Chen L, Tao J, Zhang Q, Guo B, Sun L, Yang P, Zheng X and Chu J 2018 Improvement performance of two-step electrodepositing Cu₂MnSnS₄ thin film solar cells by tuning Cu-Sn alloy layer deposition time *Mater. Chem. Phys.* **211** 382–8

[149] Chen L, Deng H, Tao J, Sun L, Yang P and Chu J 2017 Effect of the post-selenization time on the structural and optical properties of Cu₂MnSn(S,Se)₄ thin films synthesized by sol-gel technique *Mater. Lett.* **201** 185–8

[150] Lie S, Sandi M I, Tay Y F, Li W, Tan J M R, Bishop D M, Gunawan O and Wong L H 2018 Improving the charge separation and collection at the buffer/absorber interface by double-layered Mn-substituted CZTS *Sol. Energy Mater. Sol. Cells* **185** 351–8

[151] Li X, Hou Z, Gao S, Zeng Y, Ao J, Zhou Z, Da B, Liu W, Sun Y and Zhang Y 2018 Efficient optimization of the performance of Mn²⁺-doped kesterite solar cell: machine learning aided synthesis of high efficient Cu₂(Mn,Zn)Sn(S,Se)₄ solar cells *Sol. RRL* **2** 1800198

[152] Orletskii I G, Mar'yanchuk P D, Solovan M N, Maistruk E V and Kozyarskii D P 2016 Peculiarities in electrical and optical properties of Cu₂Zn₁₋ₓMnₓSnS₄ films obtained by spray pyrolysis *Tech. Phys. Lett.* **42** 291–4

[153] Chen L, Deng H, Cui J, Tao J, Zhou W, Cao H, Sun L, Yang P and Chu J 2015 Composition dependence of the structure and optical properties of Cu₂MnₓZn₁₋ₓSnS₄ thin films *J. Alloys Compd.* **627** 388–92

[154] Kesterite Mineral Data www.webmineral.com/data/Kesterite.shtml#.XIBXX4oo-M8

[155] Ghosh A, Thangavel R and Rajagopalan M 2014 First-principles study of structural stability and optical properties of Cu₂XSnY₄ (X = Fe, Co, Ni; Y = S, Se) for photovoltaic applications *energy environ Focus* **3** 142–51

[156] Kevin P, Malik M A, McAdams S and O'Brien P 2015 Synthesis of nanoparticulate alloys of the composition Cu(2)Zn(1-x)Fe(x)SnS(4): structural, optical, and magnetic properties *J. Am Chem. Soc.* **137** 15086–9

[157] Prabhakar R R, Huu Loc N, Kumar M H, Boix P P, Juan S, John R A, Batabyal S K and Wong L H 2014 Facile water-based spray pyrolysis of Earth-abundant Cu₂FeSnS₄ thin films as an efficient counter electrode in dye-sensitized solar cells *ACS Appl. Mater. Interfaces* **6** 17661–7

[158] Kumar M S, Madhusudanan S P and Batabyal S K 2018 Substitution of Zn in Earth-abundant Cu₂ZnSn(S,Se)₄ based thin film solar cells–a status review *Sol. Energy Mater. Sol. Cells* **185** 287–99

[159] Meng X, Deng H, He J, Sun L, Yang P and Chu J 2015 Synthesis, structure, optics and electrical properties of Cu₂FeSnS₄ thin film by sputtering metallic precursor combined with rapid thermal annealing sulfurization process *Mater. Lett.* **151** 61–3

[160] Chatterjee S and Pal A J 2017 A solution approach to p-type Cu₂FeSnS₄ thin-films and pn-junction solar cells: role of electron selective materials on their performance *Sol. Energy Mater. Sol. Cells* **160** 233–40

[161] Park J-Y, Noh J H, Mandal T N, Im S H, Jun Y and Seok S I 2013 Quaternary semiconductor Cu₂FeSnS₄ nanoparticles as an alternative to Pt catalysts *RSC Adv.* **3** 24918

[162] Yan C, Huang C, Yang J, Liu F, Liu J, Lai Y, Li J and Liu Y 2012 Synthesis and characterizations of quaternary Cu₂FeSnS₄ nanocrystals *Chem. Commun.* **48** 2603

[163] Dong C, Meng W, Qi J and Wang M 2017 Cu₂FeSnS₄ nanocrystals as effective electron acceptors for hybrid solar cells *Mater. Lett.* **189** 104–6

[164] Hannachi A, Oueslati H, Khemiri N and Kanzari M 2017 Effects of sulfurization on the optical properties of Cu₂ZnₓFe₁₋ₓSnS₄ thin films *Opt. Mater. (Amst)* **72** 702–9

[165] Fontané X, Izquierdo-Roca V, Saucedo E, Schorr S, Yukhymchuk V O, Valakh M Y, Pérez-Rodríguez A and Morante J R 2012 Vibrational properties of stannite and kesterite type compounds: Raman scattering analysis of Cu₂(Fe,Zn)SnS₄ *J. Alloys Compd.* **539** 190–4

[166] Khadka D B and Kim J 2014 Structural transition and band gap tuning of Cu₂(Zn,Fe)SnS₄ chalcogenide for photovoltaic application *J. Phys. Chem. C* **118** 14227–37

[167] Collord A D, Xin H and Hillhouse H W 2015 Combinatorial exploration of the effects of intrinsic and extrinsic defects in Cu₂ZnSn(S,Se)₄ *IEEE J. Photovoltaics* **5** 288–98

[168] Eisenbarth T, Caballero R, Kaufmann C A, Eicke A and Unold T 2012 Influence of iron on defect concentrations and device performance for Cu(In,Ga)Se₂ solar cells on stainless steel substrates *Prog. Photovoltaics Res. Appl.* **20** 568–74

[169] Pianezzi F, Nishiwaki S, Kranz L, Sutter-Fella C M, Reinhard P, Bissig B, Hagendorfer H, Buecheler S and Tiwari A N 2015 Influence of Ni and Cr impurities on the electronic properties of Cu(In,Ga)Se₂ thin film solar cells *Prog. Photovoltaics Res. Appl.* **23** 892–900

[170] Wang T-X, Li Y-G, Liu H-R, Li H and Chen S-X 2014 Flower-like Cu₂NiSnS₄ nanoparticles synthesized by a facile solvothermal method *Mater. Lett.* **124** 148–50

[171] Kamble A, Mokurala K, Gupta A, Mallick S and Bhargava P 2014 Synthesis of Cu₂NiSnS₄ nanoparticles by hot injection method for photovoltaic applications *Mater. Lett.* **137** 440–3

[172] Sarkar S, Das B, Midya P R, Das G C and Chattopadhyay K K 2015 Optical and thermoelectric properties of chalcogenide based Cu₂NiSnS₄ nanoparticles synthesized by a novel hydrothermal route *Mater. Lett.* **152** 155–8

[173] Ozel F 2016 Earth-abundant quaternary semiconductor Cu₂MSnS₄ (M = Fe, Co, Ni and Mn) nanofibers: fabrication, characterization and band gap arrangement *J. Alloys Compd.* **657** 157–62

[174] Yang C L, Chen Y H, Lin M, Wu S L, Li L, Liu W C, Wu X S and Zhang F M 2016 Structural, optical and magnetic properties of Cu₂NiSnS₄ thin films deposited by facile one-step electrodeposition *Mater. Lett.* **166** 101–4

[175] Rondiya S, Wadnerkar N, Jadhav Y, Jadkar S, Haram S and Kabir M 2017 Structural, electronic, and optical properties of cu₂NiSnS₄: a combined experimental and theoretical study toward photovoltaic applications *Chem. Mater.* **29** 3133–42

[176] Ghosh A, Chaudhary D K, Biswas A, Thangavel R and Udayabhanu G 2016 Solution-processed Cu₂XSnS4 (X = Fe, Co, Ni) photo-electrochemical and thin film solar cells on vertically grown ZnO nanorod arrays *RSC Adv.* **6** 115204–12

[177] Kim S, Park J-S and Walsh A 2018 Identification of killer defects in kesterite thin-film solar Cells *ACS Energy Lett.* **3** 496–500